Polarized ambient noise on Mars

E. Stutzmann[1], M. Schimmel[2], P. Lognonné[1], A. Horleston[3], S. Ceylan[4], M. van Driel[4], S. Stahler[4], B. Banerdt[5], M. Calvet[6], C. Charalambous[9], J. Clinton[4], M. Drilleau[1,7], L. Fayon[8], R.F. Garcia[7], D. Giardini[4], K. Hurst[5], A. Jacob[1], T. Kawamura[1], B. Kenda[1], L. Margerin[6], N. Murdoch[7], M. Panning[5], T. Pike[9], J.-R. Scholz[10], A. Spiga[11]

[1]Université de Paris, Institut de Physique du Globe de Paris, CNRS, Paris, France
[2]CSIC-ICTJA, Barcelona, Spain
[3]University of Bristol, UK
[4]ETH, Zurich, Switzerland
[5]Jet Propulsion Laboratory, California Institute of Technology, Pasadena, CA, USA
[6]IRAP, CNRS, Toulouse, France
[7]ISAE-SUPAERO, Toulouse University, Toulouse, France
[8]Space Exploration Institute, Neuchâtel, Switzerland.
[9]Imperial college, London, UK
[10]Max Planck Institute, Gottengen, Germany
[11]Laboratoire de Météorologie Dynamique / Institut Pierre-Simon Laplace (LMD/IPSL), Sorbonne Université, Centre National de la Recherche Scientifique (CNRS), École Polytechnique, École Normale Supérieure (ENS)

Key Points:

- Seismic noise on Mars is polarized.
- Noise polarization is in the horizontal plane at low frequency (0.03-0.3 Hz) and in the vertical plane at high frequency (0.3-1 Hz).
- Polarization azimuth varies with local time and season.
- More polarized signals are measured at low frequency than at high frequency with little variations between night and day.
- Aseismic and seismic origin of the noise are investigated

Corresponding author: Eléonore Stutzmann, `stutz@ipgp.fr`

Abstract

Seismic noise recorded at the surface of Mars has been monitored since February 2019, using the seismometers of the InSight lander. The noise on Mars is 500 times lower than on Earth at night and it increases during the day. We analyze its polarization as a function of time and frequency in the band 0.03-1Hz. We use the degree of polarization to extract signals with stable polarization whatever their amplitude. We detect polarized signals at all frequencies and all times. Glitches correspond to linear polarized signals which are more abundant during the night. For signals with elliptical polarization, the ellipse is in the horizontal plane with clockwise and anti-clockwise motion at low frequency (LF). At high frequency (HF), the ellipse is in the vertical plane and the major axis is tilted with respect to the vertical. Whereas polarization azimuths are different in the two frequency bands, they are both varying as a function of local time and season. They are also correlated with wind direction, particularly during the day. We investigate possible aseismic and seismic origin of the polarized signals. Lander or tether noise are discarded. Pressure fluctuation transported by environmmental wind may explain part of the HF polarization but not the tilt of the ellipse. This tilt can be obtained if the source is an acoustic emission in some particular case. Finally, in the evening when the wind is low, the measured polarized signals seems to correspond to a diffuse seismic wavefield that would be the Mars microseismic noise.

Plain Language Summary

Seismic noise at the surface of Mars was unknown until the first measurements by the seismometers from the InSight mission in January 2019. On Earth, the microseismic noise is dominantly composed of Rayleigh waves generated by numerous sources in the ocean. On Mars, because there is no ocean, seismic noise in that frequency band is much lower and can reach a level 500 times lower than on Earth at night. The noise polarization on Mars is also more complex than on Earth. For signals with elliptical polarization, the ellipse is in the horizontal plane with clockwise and anti-clockwise motion at low frequency (LF). At high frequency (HF), the ellipse is in the vertical plane and the major axis is tilted with respect to the vertical. The polarization azimuths are varying as a function of local time and season and they are correlated with wind direction. We investigate possible aseismic and seismic sources. Pressure fluctuation transported by wind and/or acoustic emission are possible sources of the HF polarized signals. In the evening when the wind is low, the measured polarized signals seems to correspond to a diffuse seismic wavefield that would be the Mars background noise.

1 Introduction

The Insight mission landed on the planet Mars on November 2019 (Banerdt et al., 2020; Lognonne et al., 2020) and deployed a seismic package (SEIS) which have recorded continuous seismic signals since February 2019. Seismic noise level is a crucial parameter for the success of the mission because marsquakes can only be detected when their amplitude is above the station noise level (Giardini et al., 2020). Seismic noise is also of interest in itself to determine the corresponding natural phenomena that excite the noise wavefield on Mars. It may correspond to propagating waves from sources yet to be discovered or it may be partly or completely controlled by environmental local effects. The origin of these local effects was extensively studied and modeled prior the mission launch and might be related to pressure ground deformation (Lognonné & Mosser, 1993), thermal effects (Van Hoolst et al., 2003), lander induced noise (Murdoch et al., 2017) and was summarized and reviewed by (Mimoun et al., 2017). If Mars seismic noise contains propagating waves, the noise can moreover be used to investigate the planet interior, from local scale (Romero & Schimmel, 2018), to global scale (Schimmel et al., 2011a; Nishikawa et al., 2019).

The seismic noise spectrum on Earth has a characteristic shape that can be observed everywhere on continents, on islands or at the ocean bottom (Stutzmann et al., 2009). The Earth noise spectrum has two peaks around 0.14 and 0.07 Hz called secondary and primary microseisms and a minimum between 0.05 and 0.005 Hz called hum. Sources of microseisms and hum are related to the ocean wave activity (e.g. Hasselmann (1963); Stutzmann et al. (2012); Ardhuin et al. (2015)). As there is no fluid ocean on Mars, similar microseisms and hum sources do not exist. Below 0.002 Hz, noise on Earth is caused by free air and inertial effects exerted by atmospheric perturbations on the sensor mass (Zürn & Wielandt, 2007). The density of Mars' atmosphere close to the surface is about 100 times fewer than on Earth, yet atmosphere-induced seismic signal, especially ground deformation induced by vortex-induced pressure drops have been reported by SEIS (Banerdt et al., 2020; Lognonne et al., 2020; Kenda et al., 2020; Garcia et al., 2020), as suggested by the pre-launch modeling and Earth tests (Lorenz et al., 2015; Kenda et al., 2017; Murdoch et al., 2017).

In 1976, a first seismometer recorded the seismic noise on Mars in the framework of the Viking mission (Anderson et al., 1977). The seismometer was located on the top of the lander and therefore it mostly recorded the response of the lander to the wind. To overcome this problem which was also recorded prior SEIS deployment (Panning et al., 2020), the SEIS seismometers were placed on the ground and covered by a Wind and Thermal Shield (WTS).

To determine the nature of the seismic noise recorded on Mars, one way is to analyze its polarization. On Earth, the strongest signals that compose the noise are Rayleigh waves and therefore the noise polarization is elliptical in the vertical plane (Haubrich & McCamy, 1969; Tanimoto & Rivera, 2005; Tanimoto et al., 2006). The ellipse back azimuth gives the direction toward the sources. Due to the continuously changing ocean wave activity, each seismic station simultaneously records Rayleigh waves from multiple sources. Therefore, statistical methods have been developed to analyze the noise polarization and investigate the sources (Schimmel et al., 2011b; Stutzmann et al., 2009).

To address the question of the nature of the seismic noise recorded on Mars, we monitor the continuous signal recorded by the three components of the broadband seismometer, SEIS, over the first year of the Insight mission. We restrict our analysis to below 1Hz, since initially 3 component continuous data was collected at the 2 sample per second sampling rate. We show that the polarization on Mars is very different than on Earth and that we cannot identify Rayleigh waves. We characterize the Mars noise polarization as a function of frequency and local time using a statistical approach. Finally we quantify the environmental local effect on the noise.

2 Insight mission seismic data

On November 26th 2018, Insight (Banerdt et al., 2020; Lognonne et al., 2019, 2020) landed on Mars. The lander is located in Elysium Planitia (Golombek et al., 2020), close to the equator (4.502°N, 135.623°E) in a flat area at an elevation of -2613.4 m with respect to the MOLA geoid. The topography map (Figure 1, top) shows that the structure is flat around the station toward the North and that the topography is higher with large craters toward the South.

In January 2019, the 3-component broadband and short period seismometers SEIS were placed on the ground, and a few weeks later they were covered by a Wind and Thermal Shield (WTS). Figure 1 (bottom) shows a sketch of the Insight station where we see that the lander is located to the North of the seismometers SEIS. The distance between SEIS and the lander feet ranges from 1.81 m to 3.63 m. The other instrument on the ground (HP^3, the Heat Flow and Physical Properties Package) is to the East of SEIS. These azimuths and distances are important for the interpretation of the noise polarization.

Since mid February 2019, the three components of the SEIS broadband seismometer have continuously recorded the ground motion. We present here the analysis of the continuous broadband seismic data (from Mars SEIS data service), from February 18, 2019 to April 13, 2020 which corresponds to sol 81 to 491. One sol is one day on Mars and it corresponds to 24 hours and 37 minutes UTC. Sol 0 is the day InSight landed on Mars. Our analysis is restricted to frequencies below 1 Hz. The three components U, V, W of the broadband seismometer are corrected from the instrumental response and rotated to obtain the Z, N and E components. Data display similar characteristics every sol and figure 2 shows the 3 components of the ground velocity recorded by the broadband seismometer for two sols, 210 (June 30, 2019) and 310 (October 10-11, 2019) filtered between 0.03 and 1 Hz. We observe large amplitude during the day and much weaker amplitude at night on the 3 components. We also see numerous transient signals that are mostly glitches (Lognonne et al., 2020; Scholtz et al., 2020) or dust devils and wind gusts (Banerdt et al., 2020; Lognonne et al., 2020; Kenda et al., 2020).

Daily spectrograms are computed and figures A1-A3 in the appendix show spectrograms for sol 210 and 310 in which we observe similar diurnal variations for the 2 sols. Figure 3 (top plots) shows the median Power Spectral Density (PSD) and its standard deviation in the frequency range 0.03-1Hz, computed over sol 82 to 491. For comparison, the Earth low noise model is plotted with dashed line (Peterson, 1993). The vertical PSD reaches a minimum of -190 dB in acceleration that is more than 50 dB (320 times) lower than the Earth LNM. The median PSD as a function of frequency has a V-shape that is very different to the noise PSD on Earth. Whereas the noise curve on Earth is known to be related to primary and secondary microseisms, the origin of the V-shaped noise curve on Mars is an open question. Comparing the 3 components, the minimum PSD is at 0.15 Hz for the vertical component and shifted toward 0.3-0.4 Hz on the 2 horizontal components. Finally, the horizontal median PSD is above the Earth LNM for frequencies lower than 0.6 Hz.

The median of the spectrograms as a function of local hour is shown in figure 3 (bottom plots) together with the standard deviation. For all 3 components, the minimum PSD is reached in the evening (16:00-24:00) with values of -200 to -210 dB, and then in the morning (0:00-5:00) with -200 to -205 dB. The noise PSD is higher during the day (5:00-16:00) for all 3 components in the entire frequency band. Considering the pattern as a function of frequency, we see that above 0.3 Hz all 3 components have a similar amplitude and therefore polarization analysis is required to further investigate the particle motion. Below 0.3 Hz, the horizontal components have higher amplitude than the vertical component and therefore the polarization will be mostly in the horizontal plane. Nevertheless, the similar noise amplitudes on the two horizontal components suggests that there is no systematic bias in either of the horizontal components and that they can be used to determine the azimuth of the ground motion.

3 Polarization method

The polarization describes the three-dimensional particle ground motion at the station considering seismic records along the three directions (north-south, east-west, and vertical up-down). Schimmel et al. (2011b) proposed a method to analyze noise polarization as a function of time and frequency. As the noise on Earth is dominantly Rayleigh waves, they selected only signals with elliptical polarization in the vertical plane. For Mars, we extended this method to analyze linear and elliptical polarization in any direction.

The three component signals are converted into time-frequency space using the S-transform (Stockwell et al., 1996) The eigen-analysis of the cross-spectra matrix for each time-frequency gives the instantaneous polarization attributes such as the semi-major and semi-minor vectors of the ellipse that best fit the ground motion. The planarity vector is defined as the cross product of the semi major and minor vectors and it is perpendicular to the ellipse plane. This vector contains also the information on the orientation of the particle motion which moves along the ellipse from the semi-major to the semi-minor along the shortest path. This motion can be pictured using the right-hand rule. If the right-hand thumb points into the direction of the planarity vector then the fingers curl along the orientation of the motion. Figure 18 shows the ellipse (red curve), semi-major (x'), semi-minor (y'), planarity (z') vectors, and orientation of the particle motion.

In order to measure the stability of the polarization at each time-frequency, we compute the instantaneous degree of polarization (Schimmel & Gallart, 2003, 2004). The degree of polarization (DOP) is an instantaneous quality measure based on the stability of an arbitrary polarization state with time. It is based on the fact that a high quality signal should not vary its polarization through the course of the signal or equivalently through a small sliding data window (Schimmel et al., 2011b). We first compute the mean planarity vector over a given analysis data window (equivalent to a given duration of the signal). The DOP is then determined as the normalized sum of the scalar products between the instantaneous planarity vectors and the mean planarity vector. The DOP is equal to 1 for stable polarized signals and reaches 0 when the polarization is random. For linear polarization, the planarity vector is replaced by the semi-major vector for computing the DOP. Azimuths are measured from North toward East, that is from 0 to 180°, and there is an ambiguity of ±180°.

This approach enables us to extract signals with stable polarization over time. The detected signals can have large or weak amplitude. Weak signals with stable polarization will be extracted whereas more energetic signals with less stable polarization over time will be discarded. This approach is designed to extract polarized signals from a complicated wavefield, composed of a zoology of signals. Note that weak signals may not be detected with other methods based on a different definition for the degree of polarization (e.g. Samson and Olson (1980)).

4 Polarization analysis

We present the polarization attributes from when the seismometers were covered with the Wind and Thermal Shield, i.e. after sol 81. We start with the polarization analysis of data shown in Figure 2, for sol 210 and 310. Figure 4 (top) shows that the degree of polarization (DOP) is above 0.5 almost everywhere, which means that there are signals with stable polarization at most frequencies and during the entire sol. The polarization is more stable (DOP larger than 0.85) at low frequencies below 0.3 Hz, and mostly during the day (7:00 to 18:00). The exact start and end time of this diurnal stable polarization is slightly different between sol 210 and 310. We also observe high DOP in the early morning (around 5:00) for both sols, and in the evening between 22:00 and midnight only for sol 210.

Figure 4 (bottom) shows the linearity of the polarization. We see that the polarization is mostly elliptical for frequencies above 0.3 Hz and slightly more linear at lower frequencies. We also see yellow vertical lines which correspond to signals linearly polarized in the entire frequency band for short duration. They mostly correspond to transient features or glitches that are clearly visible on the seismograms (Figure 2).

In order to better understand the noise polarization, we analyze separately linear and elliptical polarized signals. If the noise contains seismic waves, the corresponding polarization can be linear or elliptical. Body waves have mostly linear polarization whereas Rayleigh waves have elliptical polarization in the vertical plane. Nevertheless, in the case of interference of seismic waves from multiple directions, ground motion polarization becomes more complex.

We start with the linear polarization. We select signals with linearity higher than 0.97 and Figure 5 shows their incident angle and azimuth as a function of time and frequency for sol 210 and 310. Vertical lines visible on both the incident angle and the azimuth plots mostly correspond to the numerous glitches that can be identified on the seismic traces. The number of glitches varies from one day to another but they are more abundant at night. The azimuths are E-W in the morning and N-S at sunset. We remind the reader that azimuths are measured $\pm 180°$. Glitch origin is still under debate (Lognonne et al., 2020; Scholtz et al., 2020). Apart from these signals visible in the entire frequency range, we also observe changes of polarization between day and night and between high and low frequencies. During the day and below 0.3 Hz, the detected signals are linearly polarized in the horizontal plane (incident angle close to 90°) with azimuth toward all directions. Those signals likely correspond to atmospheric sources and might be associated to pressure-induced ground tilts (Kenda et al., 2020; Garcia et al., 2020). At higher frequency (above 0.3 Hz), the incident angles are tilted with respect to the vertical axis, with an angle of about 60°. At this stage it is not possible to determine the origin of these linear signals but a lander origin is likely, as proposed prior to launch (Murdoch et al., 2017).

We then investigate signals with elliptical polarization and select signals with linearity lower than 0.9. In order to determine the orientation of the polarization ellipse in the 3-D space, Figure 6a shows, for sols 210 and 310, the incident angle of the semi-major vector, the angle between the ellipse and the vertical plane and the azimuth of the major axis. The most striking feature in Figure 6 is the difference of elliptical polarization above and below 0.3 Hz. Below 0.3 Hz, the major axis incident angle is close to 90°, that is horizontal (Figure 6a, top plots). The angle between the ellipse plane and the vertical plane (Figure 6a, middle plots) is close to +90° or -90°. This means that the particle motion is elliptical in the horizontal plane with clock-wise and anti-clockwise motion during the entire sol. The only change in this frequency band is the azimuth which is rotating over the day (Figure 6a, bottom plots). On sol 210, the azimuths are toward N40E to N90E in the morning before 7:00, then they rotate to angles between 0 to N60E during the day (7:00 to 18:00). Around sunset, they are close to 120°, and at the end of the sol, they are again similar to morning azimuths. We observe similar azimuth variations on sol 310, but the time of azimuth changes are slightly shifted.

Above 0.3Hz, Figure 6a shows that the major axis incident angle is tilted with an angle of about 50° with respect to the vertical (top plots). The middle plot shows that the ellipse is in the vertical plane (angle of 0°). Finally, the ellipse azimuths are toward N120E-N140E during the day and no consistent azimuth can be determined at night. One striking feature is the change of polarization in the evening (18:00-21:00) which is more similar to what is observed at lower frequency. We note that it corresponds to the time when the signal amplitude is the lowest on the three components (Figure 3).

Figure 6b summarizes the elliptical polarization: above 0.3 Hz, the ellipse is in the vertical plane and the major axis is tilted with respect to the vertical axis; below 0.3 Hz, the ellipse is in the horizontal plane with clockwise and anti-clockwise motion. These particle motions are far more complex than what we observe on Earth and, at this stage, propagating waves cannot be easily identified.

We similarly investigated all available data and observed that the discrepancy between high and low frequency patterns is visible every sol. Figures A1 to A4 in the appendix show the frequency dependent particle motion azimuths from sol 82 to 491, which corresponds to more than one year on Earth. To summarize these figures, we selected a high frequency band (0.7-0.9 Hz) and a low frequency band (0.1-0.2 Hz) and computed azimuth histograms as a function of time. Figure 7 shows the most abundant azimuths as a function of local time and sol. We retrieve the azimuth differences between day and night as in Figure 6 but we also see progressive changes of these azimuths as a function of increasing sols. Let us first consider the LF band. About one hour after sunrise on the first sol (82), the azimuth changes abruptly from 60° to 0°. Later between sols 170 and 450, around sunrise the azimuths vary progressively from 60 to 110^o before the same abrupt change. During the day, we also see progressive changes of the azimuths with increasing sols. One hour before sunset, the azimuth becomes dominantly N-S. At HF, azimuths are more scattered which can be confirmed by looking at the daily plots (Figure A1 to A4). The azimuths are different from those at LF but they also progressively change with increasing sol. They are around 150° in the morning, progressively change to 60° around sunrise, then change abruptly to 120° one hour after sunrise, and progressively change again to 0° just before sunset and remains very scattered from sunset to midnight. During part of the conjunction there were no data returned from InSight. Just after it, and up to sol 370, we observe for both HF and LF that, just before sunset, the polarization azimuths are around 60°. The azimuth similarity every sol and their progressive changes with increasing sols, may indicate that the detected signals are related to daily and seasonal changes. It may also indicate that these signals are not generated at the lander since it does not change its position.

Finally we investigated variations of the number of detected signals. Figure 8 shows the number of polarized signal detected per hour as a function of frequency for sol 210 and 310. The absolute numbers depend on the definition of when a signal polarization is considered stable and are not important here as we compare only relative variations. We only considered signals with elliptical particle motion in order to exclude glitches. More polarized signals are detected at low frequency than at high frequency. After a minimum between 0.2 and 0.8 Hz, the number of detections increases again at higher frequency. We further see that at low frequency (below 0.3Hz), we detect a similar amount of polarized signals at day and night. At high frequency (0.3-0.8 Hz), slightly more polarized signals are detected during the day and a bit less in the evening. We also observe some variability of the number of detections between sol 210 and 310. Finally, considering the entire frequency band, we do not detect significantly more signals during the day.

5 Discussion

Our key observations are different elliptical polarization patterns above and below 0.3 Hz, azimuth changes over LMST hour that are different in the 2 frequency bands and slowly vary over sols and, a similar amount of polarized signals during day and night at low frequency and slightly more during the day at high frequency. The polarization ellipse is in the horizontal plane below 0.3 Hz and tilted in the vertical plane above 0.3 Hz.

On Mars, the seismic noise is likely generated by different phenomena related to local wind and pressure. Figure 9 shows for sol 210 and 310, the pressure filtered in the same frequency band as seismic data (0.03-1 Hz) together with the wind speed and wind azimuth as a function of local time. The pressure fluctuates a lot during the day and much less at night (Banfield et al., 2020). We observe a steady increase of wind speed from after sunrise to sunset, high wind with high variability during the day, and the wind almost stops in the evening (the "quiet zone" described e.g. in Banfield et al. (2020)). Figure 10 shows the relation between the wind speed and the three components of the seismic root mean square (rms) amplitudes as a function of LMST. Larger seismic amplitudes are observed for higher wind speeds. Furthermore the major vector azimuth of the polarization ellipse is relatively well correlated with the wind direction as will be shown further below.

Before investigating the possible origins of the measured polarized signals, we recall here the relationship between measured seismic amplitude and wind speed as proposed in the Supplement of Giardini et al. (2020):

$$n^2 = \left(e^2 + \left(0.0058\frac{< v^2 >}{f^2} + 0.44 f^2 < v^2 >^2\right)\right) 10^{-20}\ m^2/s^4/Hz\ , \tag{1}$$

where n^2 is the seismic signal PSD, $< v^2 >$ is the mean squared wind speed, e is the instrument self noise (Lognonne et al., 2019), and f the frequency. Wind strength dependency is furthermore developed in Charalambous et al. (2020). The noise amplitude roughly follows a wind dependency at low frequency of $\sqrt{< v >^2}$ and of $< v >^2$ at high frequency. The frequency for which the two regimes equal depends on the wind speed and is about 0.3 Hz, 0.2 Hz and 0.1 Hz for winds of 1.25 m/s, 3 m/s and 10 m/s respectively. In our polarization analysis, the frequency of about 0.3 Hz is the frequency that separates the two types of elliptical polarization either in the horizontal or the vertical plane.

In the following we focus on the origin of the measured polarized signals, which can be aseismic or seismic. Aseismic phenomena can be (1) instrument self noise, (2) sensor assembly and/or tether induced noise, (3) lander and wind shield noise, (4) local pressure and wind effects. On the other hand, seismic polarized signals are due to propagating waves generated by natural sources. These sources may be in the atmosphere (5) or the solid planet (6). Let us now go through the different aseismic and seismic candidates for the observed signals in more details.

5.1 Instrument self noise

In the evening and at high frequency, when the lowest noise PSD is reached (Figures 3, A.5 and A.6 in supplementary material A), the signal amplitude is close to the self noise of the instrument (Lognonne et al., 2020). At frequencies larger than 0.01 Hz, the self noise of each axis is however non-coherent in relation to the displacement transducers and feedbacks of the VBBs (Lognonne et al., 2019) and can not generate any stable elliptical polarization.

5.2 Sensor assembly and tether induced noise

The lander and the sensor assembly (SA) are connected through the tether and the Load Shunt Assembly (LSA). The LSA serves as a buffer to disconnect lander and tether motions from the SA. The LVL is the leveling system of the SA capable of tilting the SA for centering and calibration purposes. The lowest and more damped mode frequencies of the LSA are about 5 Hz and 8 Hz with low Q under Earth gravity and zero-slope condition (Lognonné et al., 2019). The mode frequencies of the LVL are much higher, 40 Hz or more and with larger Q of about 10 (Fayon et al., 2019). The modes of the LSA were measured on Mars during the last move of the pinning mass. The torsional mode of the LSA (9.5 Hz, Q = 13) and the longitudinal modes (2.86 Hz, 5.3 Hz, Q = 25-35) were again detected with different Qs. Future works will detail further the on-Mars calibrations.

A wind interaction with the tether or a wind interaction with the lander transmitted through the tether will generate a linear signal that is transmitted to the LSA and then to the SA. This signal will be attenuated as $\frac{\omega_{LSA}^2}{\omega_{LVL}^2}$ but will have a significant phase delay equal to the 1/Q difference between the LSA modes contributing mostly to the N, E and Z directions.

The coherency of the seismic signals recorded on the vertical and horizontal direction could be associated to tilts or small rotation of the sensor assembly (SA). These tilts or rotations are generated by the SA interaction with the environment, including reaction to forces generated by the tether and not damped by the LSA. The three components of these coherent signals are however transmitted by LSA modes with different longitudinal, vertical and transverse transfer functions. As soon as these modes have different Q, this can generate phase delay between the two horizontal components and the vertical one. Although this will require a complete and detailed modeling to confirm, the phase delay is roughly equal to the difference of 1/Q between the LSA modes.

In the following, we test whether such configuration can explain the measured polarization for frequencies above 0.3 Hz, that is the inclined semi-major vector of the vertically polarized ellipses. In principle, the sum of an elliptical polarized signal with vertical or horizontal semi-major axis and a linear polarized signal with inclined motion can cause a signal with elliptical polarization and inclined semi-major axis. Therefore, we decomposed the measured elliptically polarized signals into the sum of an elliptical polarized component in the V-H plane and a linearly polarized component with small phase shift with respect to the elliptical ones. The decomposition process is described in Appendix A.

This decomposition can be made for any phase delay between the elliptical and linear motion, the latter remaining not constrained by this decomposition. We took a phase delay of 0.15 radian corresponding to the phase shift between the torsional mode of the LSA (Q = 13) and the longitudinal or vertical modes (Q = 25-35) as measured during the pinning mass adjustment on Mars which excited the LSA modes (Hurst et al., manuscript in preparation). We restrict here the analysis to polarized signals with a small B/A ratio, (in the range of 0.05-0.15), that corresponds to linearity between 0.85 and 0.95. Results are shown in Figure 11.

The most interesting observation is a clustering of the azimuths of the elliptical component in the 30-40° range and its perpendicular, between 120-130° with respect to the North. The first angle range is toward one foot of the SA. The H/V ratio of the elliptical components are mostly smaller than 1 above 0.5 Hz but tend to be larger than 1 at low frequencies. All the signals have a linear component with larger energy than the elliptical one. These results support the phase delay between the longitudinal, vertical and transverse reactions of SEIS's LSA as a candidate for part of the small ellipticity signal (in the range of 0.85-0.95 in linearity). But very large phase shifts (e.g. signal with linearity smaller than 0.85) seem difficult to be explained by the LSA quality factors. A full amplitude model of the possible tether/LSA noise injection remains to be made.

5.3 Lander and wind shield generated noise

Both lander and wind-shield motions induced by wind are known to be sources of noise generating larger vertical than horizontal seismic amplitudes above ∼0.3 Hz, as was suggested in pre-launch studies (Murdoch et al., 2017, 2018). The lander-generated noise is expected to be 4 times larger than the noise caused by the wind shield. The excitation source is mostly wind drag on the lander and wind shield and therefore has a v^2 (eq. 1) dependency for the high frequency noise. In addition to that, the lander also generates resonances observed above 1 Hz (Lognonne et al., 2020; Giardini et al., 2020), which are above the frequency range of this study.

The drag noise is generated through static loading on the ground of both the three lander feet and the wind shield. The drag of the wind shield generates displacement of the three axes of the SEIS seismometer. The pre-launch estimation of this noise provides, however, small noise amplitudes. For the vertical noise PSD, n_Z^2, the proposed dependency is:

$$n_Z^2 = \left(0.024\left(\frac{v_{s0}}{v_s}\right)^2 < v^2 >^2 \ f^{2/3}\right) \ 10^{-20} m^2/s^4/Hz \ , \tag{2}$$

where we set the wind-square rms $< v^2 >$ of the 95% day level to 7.2^2 m^2/s^2, as obtained from the integration of the wind-squared amplitude spectrum between 0.1 mHz and 1 Hz and where v_s is the ground shear velocity, while $v_{s0} = 150 m/s$ is the reference velocity used by Murdoch et al. (2017) and f is the frequency in Hz. Taking into account ground shear velocities of about 70 m/s, the model provides both smaller vertical noise than observed (by a factor of 2 in amplitude), as well as a different frequency dependency in the high frequency regime, although the latter being related to hypothesis in the wind turbulence spectrum, to be refined with new data.

This model, however, generates no phase shifts between the E,N,Z noise components and therefore cannot cause elliptically polarized motions. Phase shifts might however be generated due to the distance between the two solar panels and the lander body. This may happen if their excitation is generated by traveling wind/pressure perturbations reaching the two solar panels at different times (i.e. with phase delay) (Murdoch et al., manuscript in preparation). The largest lander effects may then occur in the low wind night conditions, when the wind blows in the direction of the azimuth of the solar panels and at short periods where the phase shift would be maximum. In that case it is expected that the ellipticity of the polarized signals increase with frequency. This is not what we observe for three reasons. First, the high frequency linearity is not decreasing at night (Fig. 4). Second, the wind directions during night are varying with season (Spiga et al., 2018; Banfield et al., 2020). And third, we showed that the number of polarized signals between morning, evening and day is relatively comparable, even if the wind speed and azimuth are significantly changing.

In conclusion, we do not consider the lander generated noise as the primary source of polarized noise, even if a full model needs to be developed to confirm this hypothesis. Lander and WTS can nevertheless contribute significantly to the linear noise, especially those with a clear wind-square amplitude dependency, as demonstrated by Charalambous et al. (2020).

5.4 Pressure fluctuation transported by the environmental wind

We focus here on the effect of local pressure fluctuations carried by the environmental wind. During the daytime, the local pressure variations generate a compliance effect on the vertical component and tilt mostly visible on the horizontal components (Lognonne et al., 2020; Banerdt et al., 2020). Such an effect is observed on Earth at longer periods (e.g. (Roult & Crawford, 2000)) and also at the ocean bottom (e.g. (Crawford et al., 1991)). On Mars, compliance and tilt are best observed when dust-devil convective vortices pass close to the Insight station (Banerdt et al., 2020; Kenda et al., 2020). On sol 210, 34 convective vortices were detected during the day-time.

Pressure fluctuations carried by the environmental wind can generate elliptically polarized signals in the vertical plane that are distinct from the linear ground deformation due to the pressure static loading (e.g. Farrell (1972)). The noise carried by wind has been proposed as one of the major sources of VBB recorded noise below 1 Hz (Lognonné & Mosser, 1993; Lognonne et al., 2020; Garcia et al., 2020; Kenda et al., 2020). This is furthermore supported by the strong correlation of the azimuth of the polarized signals with wind direction which is particularly striking during the day in both high and low frequency bands (Figure 12). It is also illustrated in Lognonne et al. (2020) and Charalambous et al. (2020).

As shown by Sorrells (1971) and developed for Mars by Kenda et al. (2017) and Kenda et al. (2020), pressure waves propagating at wind speed c will generate a retrograde elliptically polarized signal in the vertical plane. If the pressure wave is propagating horizontally, it can be expressed as $p(x,t) = p_0 e^{i\omega(t-x/c)}$. Then, for a homogeneous half-plane, the resulting seismic signal H/Z ratio is given by:

$$\frac{H}{Z} = \frac{v_s^2 + v_p^2 \frac{g}{c\omega}}{i v_p^2} \ , \qquad (3)$$

where H and Z are the horizontal and vertical seismic displacements, v_p, v_s are the ground P and S velocities, g the martian gravity and ω the angular frequency respectively.

At some frequencies and wind velocities, this signal can therefore be comparable in polarization to a Rayleigh wave, which has a H/Z ratio of about $\frac{2}{3i}$ in an homogeneous medium. As shown by Kenda et al. (2020), a more complex, depth dependent structure will have a H/Z ratio affected to first order by larger seismic velocities due to compaction in the first 10 meters. This is illustrated in Figure 13 with the simple two-layer model developed by Kenda et al. (2020). The H/Z ratio is minimum for winds larger than 4-5 m/s close to frequency of 0.5 Hz, with H/Z amplitude ratio in the range of 0.2-0.5. This ratio is larger than one at lower frequency for almost all wind regimes. The ellipticity of the signal is therefore expected to vary with frequency and wind speed.

When compared to surface wave polarization, differences are (1) the phase velocity, (2) the correlation with pressure and (3) the variation of the H/Z with wind and (4) the H/Z amplitude ratio.

Let us now consider the dependency of linearity (L) with wind speed. We focus on sol 210 and represent the histograms of the B/A ratio of the ellipse values as a function of local time (Figure 14), where A is the semi-major and B the semi-minor axis. B/A ratio corresponds to 1-L. A clear dependency is observed, with the lowest B/A when the wind is very low, that is between 16.00 and midnight LMST (in the aforementioned "quiet zone"). This is one first argument supporting a pressure origin for at least part of the polarized signals above 0.3 Hz.

A potentially misleading observation is the lack of coherency between VBB signals and pressure signal apart from the active day time activity, as already noted in Lognonne et al. (2020), Garcia et al. (2020), Kenda et al. (2020). Figure 15 shows the coherence between each seismic component and pressure in 1 hour windows. It illustrates that the coherency with pressure is much less during the evening and night time and at high frequencies. Coherence with pressure is low for all three components of frequencies above 0.3 Hz day and night. The coherence is also low below 0.3 Hz at night when the pressure variability is low. During the day, the coherence with pressure increases between 0.04 and 0.2 Hz, and the largest effect is observed on the vertical component.

The lack of coherence must however be taken with care in any argument rejecting pressure waves during the evening or night. This is illustrated by Figure 16 which shows, based on the VBB mean noise shown by Lognonne et al. (2020), the amplitude of the pressure fluctuations necessary to generate these noise levels. Only those during the day time are well above the minimum noise level of the pressure sensor reported by Banfield et al. (2020). That minimum noise level can be either the pressure sensor self-noise or other source of pressure fluctuation not generating seismic polarized ground deformation. In all cases, and if we assume that Sorrells noise is a potential source above 0.2 Hz, this will explain the lack of coherence during the evening and night between the VBB signal and the pressure signal.

Sorrells' theory predicts seismic noise polarization that is frequency-dependent. This frequency dependence comes from the compliance model, from the propagating pressure fluctuation and from the variation of the environmental wind. In a 1D homogeneous half space, the compliance is not frequency-dependent. Considering a layered model with increasing rigidity with depth, the compliance roughly increases like $f^{0.7}$ until a corner frequency in the range of 0.5-1 Hz depending on the wind (Figure 13). For the pressure, observations suggest a slope of about -1.7 (Banfield et al., 2020) in power and -0.85 in pressure amplitude spectrum.

The two effects of compliance and pressure amplitude spectrum compensate and lead, for a stable wind, to a roughly flat spectrum in ground velocity until the corner frequency and therefore a f spectrum in acceleration until the same corner frequency. At long periods (f $\leq$ 0.1 Hz), the pressure only cannot explain the $1/f$ seismic observation and the stability of the wind needs to be considered for generating observations and/or injection of horizontal noise on the vertical, as the latter have amplitude variations like f^{-1} at long period due to tilt effects.

In conclusion, whereas the pressure waves are a good candidate for explaining the amplitude of the seismic signals and have been well-modeled for large pressure drops (Banerdt et al., 2020; Lognonne et al., 2020; Kenda et al., 2020), they cannot explain the observed polarization, neither the horizontal polarization at low frequency, nor the inclined polarization in the vertical plane at high frequency. Possibly, local lateral heterogeneities, as for instance the Homestead hollow (Golombek et al., 2020), may explain this polarization but this has not been investigated here.

5.5 Acoustic emission

Infrasonic waves have been suggested as potential candidates to explain some of the events observed by the SEIS instrument (Martire et al., 2020). Can they explain the polarized background noise of SEIS?

On Earth, winds are known to generate infrasound (Posmentier, 1974; Cuxart et al., 2016). Posmentier (1974) reported, for example, infrasound at 1 Hz of about 1500 nbar$^2/Hz$ in power (15 mPa$^2/Hz$) for wind speeds of 40 m/s at 10 km of altitude. Let us use these Earth observations for a rough estimation of the possible strength of acoustic pressure at the surface of Mars, considering a source correction term and the propagation from the source altitude to the ground of Mars.

For the source, following (Goldreich & Keeley, 1977), the emitted acoustic pressure at the source in the atmosphere is $\rho v_H^2 \left(\frac{\lambda}{H}\right)^{2/3}$, where ρ, v_H, λ and H are the atmosphere density, horizontal wind velocity, large eddies' correlation length and size, taken as comparable to the atmosphere height scale by (Goldreich & Keeley, 1977). The propagation term from the source down to the ground is $\frac{\sqrt{e^{d/H}}}{d}$, where d is the altitude of the source. We can then predict from Earth observations the expected acoustic pressure on the ground on Mars.

On Mars, possible sources are the turbulent wind regimes occurring during most of the daytime within the flow predicted by general circulation models (GCM) for sols 210 and 310, with typical velocities of 20 m/s at about 1 km of altitude. The simple extrapolation presented above, for similar correlation length of eddies, gives acoustic pressure amplitude at the ground of ΔP=0.2 mPa/$Hz^{1/2}$. This value is smaller by about 20, as compared to the Earth case.

Acoustic emission in the atmosphere has a wind-squared dependency, although the wind is not the local one but the wind generating the acoustic emission. The frequency dependency of this acoustic source can be estimated with a Kolmogorov inertial-subrange model (e.g. Shields (2005)) and therefore with a frequency dependency of $f^{-7/3}$.

When such acoustic signals reach the ground at the SEIS location, they generate a reflected acoustic wave and a transmitted P and S wave in the solid planet. Can it explain part of the observed signals?

In order to estimate the amplitude and, if any, polarization properties of such acoustic emission when hitting the ground, we consider again the half space breciated bedrock model used for estimating the Sorrells pressure waves in the previous section. We consider a simple, isotherm atmosphere at 220K and 700 Pa, for which the sound speed is about 250 m/s. Reflection and Transmission coefficients are computed following (Aki & Richards, 2002) in the case of a fluid/solid interface. Note that analytical expressions are given by (Gualtieri et al., 2014; Zhang et al., 2018), as well as discussion of the critical angles for the ocean-bottom case.

The pressure to seismic wave ground velocity conversion coefficients, shown in Figure 17, are about 5 $10^{-7} m/s/Pa$ on the vertical component and comparable on the horizontal component between the two extreme critical angles, of about 15 and 30 degrees respectively. With a surface acoustic pressure of 0.2 mPa/Hz$^{1/2}$, this provides an estimated ground velocity amplitude of about 10^{-10} m/s/Hz$^{1/2}$.

Figure 17 shows that a specific feature of these incident acoustic waves is to generate, for incidence angles in the range between the two critical angles, horizontal ground displacement amplitude larger than the vertical one, as well as an elliptical polarization with a semi-major axis inclined with respect to vertical, because the H/V phase delay is different from $\pi/2$.

Figure 17 also shows that the variation of the linearity with the incidence angle starts from 1 at the first critical angle ($\sin i_{c_1} = \frac{c_{atm}}{v_P}$), decreased to about 0.6 before reaching 1 again for the second critical angle ($\sin i_{c_2} = \frac{c_{atm}}{v_S}$). It then decreases again down to 0.2 before growing again toward an almost horizontal linear polarization state. For the first critical incident angles i_{c_1}, the angle between the semi-major angle and the vertical is 90^o. For increasing incident angles, the semi-major angle with the vertical is decreasing down to 45^o, which is reached for the second critical incident angle i_{c_2}.

The angle of 45 degrees is consistent with the measured semi-major incident angle for frequency above 0.3 Hz. This angle is measured most of the time except during the very low wind period between 18:00 LMST and 22:00 LMST (Figure 6). An acoustic pressure source is therefore the only mechanism able to generate, for 1D models, ellipticity with an oblique semi-major axis with respect to vertical. However, its frequency dependency, for a Kolmogorov inertial-subrange model, is proportional to $f^{-7/6}$ for the pressure and therefore only $f^{-1/6}$ in ground acceleration. Note that during the night, wind might remain relatively large at a few kilometers altitude above the surface (the so-called low-level jet, see (Banfield et al., 2020)) and this can provide a noise background.

5.6 Propagating polarized seismic waves

Finally, let us consider seismic waves as a potential source of noise. During windy conditions – that is, from midnight to about 18:00 LMST, we have already seen that above 0.3 Hz, the polarization is elliptical and tilted in the vertical plane and below 0.3 Hz, the polarization is elliptical clock-wise and anti clockwise in the horizontal plane. In both cases, this is definitely different to the noise polarization that we observe on Earth where Rayleigh wave elliptical polarization in the vertical plane can be clearly identified (e.g. (Tanimoto & Rivera, 2005; Schimmel et al., 2011b; Stutzmann et al., 2009)).

The analysis of the measured seismic polarization on Mars suggest that a large part of the signals have wind-induced origins.It is therefore better to concentrate on the "quiet zone" time window between 18:00 and 22:00, when the local wind is extremely small and the corresponding local or regional noise source discussed above weaken.

During this time period, the degree of polarization of the signals is strongly decreasing to about 0.5 and the incident angle of the major vector is relatively close to 90 degrees (Figure 6). We also have a major change in the histogram of the B/A ratio, peaking at 0 and therefore suggesting a background of linearly polarized signals (Figure 14), relatively isotropic in azimuth. These signal may correspond to seismic propagating waves.

In summary, measured elliptical signals show an azimuthal directivity, most of the time close to the wind direction, while on the contrary, measured linear signals have much more isotropic azimuths. We believe that this low-level background noise is the only candidate for a diffuse seismic wave background noise. All events detected so far Giardini et al. (2020) have indeed shown large evidence of scattering, including below 1 Hz Lognonne et al. (2020). In its multi-diffusion limit, seismic background will therefore have about 10 times more energy in S waves than P waves (Aki (1992), Papanicolaou et al. (1996)) which therefore support mostly horizontally linearly polarized seismic waves.

6 Conclusion

Seismic noise on Mars, recorded by the Insight station during the first 480 sols of the mission, is 500 times smaller than on Earth at night and the average noise level reaches -195 dB in acceleration around 0.1 Hz. The noise level in the frequency band 0.03-1 Hz is higher during the day at all frequencies and, furthermore, the vertical axis is noisier during daytime than the horizontal.

The time-frequency polarization of seismic noise on Mars is investigated using the method developed for studying Earth noise (Schimmel et al., 2011b; Stutzmann et al., 2009). The key point is the use of the degree of polarization which enables us to extract signals with stable polarization as a function of time and frequency, whatever their amplitude. Whereas on Earth, the microseismic noise is mainly polarized as Rayleigh waves in the vertical plane, on Mars the polarization is more complex.

We measured polarized signals at all frequencies between 0.03 and 1 Hz and at all times. Linearly polarized glitches can be clearly identified and they are more abundant during the night as also observed by (Scholtz et al., 2020). Signals with elliptical polarization have different patterns at low (0.03-0.3Hz) and high (0.3-1Hz) frequencies. At low frequency, these signals are always polarized in the horizontal plane with both clockwise and anticlockwise motion. At high frequency they are polarized in the vertical plane and the major axis is tilted with respect to the vertical. The measured azimuths are different in the two frequency bands but they both strongly vary over LMST time with abrupt changes around sunset and sunrise. They also display progressive variations from one sol to another following seasonal changes, along the 480 sols of the mission. These azimuths are correlated with wind direction in both frequency ranges, particularly during the day.

We investigated the possible origins of this polarized noise. Results for the different noise source candidates are summarized in Table 1. We excluded sensor self noise and lander noise as they only generate linearly polarized signals. LSA or tether noise may only explain a small fraction of the polarized signals, which have linearity above 0.8. Compliance effect generated by pressure waves propagating along the planet surface at the wind speed is a good candidate for explaining part of the HF polarized signals. The resulting elliptical polarization is in the vertical plane as our observation above 0.3 Hz, but this mechanism cannot explain the inclined semi major axis. Finally, the only mechanism that we have found which can generate a tilt of the vertical ellipse, corresponds to acoustic waves coming from the atmosphere and hitting the ground at the SEIS location with an incident angle around 15-30^o.

Finally it is only during low wind time, that is between 18:00 and 24:00 LMST, that we can investigate the seismic background noise. The polarized signals are more linear and they have isotropic azimuths which is not the case for the rest of the sol. We consider that this low-level background noise is the only candidate for a diffuse seismic wave background noise. In the shallow layers corresponding to a multiple-diffusion medium, this seismic background noise would mostly correspond to S-waves, which is consistent with almost linear polarization in the horizontal plane. Sources of these seismic waves are still to be discovered.

	Vertical Power (10^{-20} $m^2/s^4/Hz$)	LF polarization (0.03-0.3 Hz)	HF polarization (0.3-1 Hz)	Azimuth
Observations	$e^2 + 0.0058\frac{<v^2>}{f^2} + 0.44f^2 < v^2 >^2$	ellipse in the horizontal plane	inclined ellipse in the vertical plane	varying over LMST and season
Sensor self noise	$e^2 = 0.125\ f^{-1.2} + 0.49 + 2\ f^3$	None	None	None
Lander Noise	$0.1\ \left\langle v^2 \right\rangle^2 f^{2/3}$	Linear (L = 1)	Linear (L = 1)	Lander related
LSA/Tether noise	Expected < 100 by design	0.8 < L < 1	0.8 < L < 1	Tether or feet related
Pressure waves noise	$> \frac{f^{-0.4}}{22.5} \times \left(\text{observation} - \text{e}^2\ \right)$	ellipse in the vertical plane	ellipse in the vertical plane	Toward the source
Acoustic emission noise	$0.015\ \left\langle v^2 \right\rangle^2 f^{-1/6}$	inclined ellipse in the vertical plane	inclined ellipse in the vertical plane	toward the source
Micro-seismic noise	less than acoustic emission noise	linear or elliptical	linear or elliptical	toward the source or random in scattered medium

Table 1. Summary of the noise observations and their possible sources. Observations are from Lognonne et al. (2020), Giardini et al. (2020) and this study. Sensor self noise is from Lognonne et al. (2019), with an approximation valid between 0.02Hz and 1 Hz. Lander noise is from Murdoch et al. (2017). A lower bound of the pressure noise is estimated from the ratio between day VBBZ noise and the coherent part of it with respect to the product of wind by pressure, the later recorded by APSS (see Supplement 1 of Lognonne et al. (2020)). This ratio vary from 3 at 0.1 Hz to 4.6 at 1 Hz. L is the polarization linearity. Acoustic emission noise estimation is from Earth scaling as developed in the text. Other wind related noise sources on the horizontal axis could be considered, such as wind-induced ground cooling. All frequencies are in Hz

Acknowledgments

This is the Insight contribution number 143 and IPGP contribution number XXX. We acknowledge NASA, CNES, their partner agencies and Institutions (UKSA, SSO, DLR, JPL, IPGP-CNRS, ETHZ, IC, MPS-MPG) and the flight operations team at JPL, SIS-MOC, MSDS, IRIS-DMC and PDS for providing SEED SEIS data. French authors are supported by ANR (ANR-19-CE31-0008-08) and by CNES for SEIS science support. AH is supported by the UK Space Agency through grant #ST/R002096/1. Seis data doi is $http://dx.doi.org/10.18715/SEIS.INSIGHT.XB\_2016$ associated with the InSight Mars SEIS Data Service together with IPGP, JPL, CNES, ETHZ, ICL, MPS, ISAE-Supaero, LPG, MFSC. $https://doi.org/10.18715/SEIS.INSIGHT.XB_2016$

7 Annex: Polarization decomposition

Let us consider the frame (0x'y'z') corresponding respectively to the semi-major axis, semi-minor axis and to the direction perpendicular to the elliptical particle motions. In this axis, the particle motion can be expressed as:

$$\begin{aligned} x' &= A\cos(\omega t) \ , \\ y' &= A(1-L)\sin(\omega t) \ , \\ z' &= 0. \ , \end{aligned} \tag{4}$$

where ω, A and Ł are the angular frequency, the intensity of the particle motion and the polarization linearity, respectively.

Figure 18 show a sketch of the ellipse of polarization and the Euler angles. Let us search first the three Euler angle necessary to rotate this frame into the one characterized by the polarization analysis, which characterizes the elliptical particle motion with three angles: the incidence angle of the semi-major axis x' with vertical I_P, the azimuth between North and the projection of the semi-major axis on the horizontal plane ψ_P and the angle between the perpendicular to the plane x'-y', therefore z' with the horizontal plane θ_P. The nutation angle θ is equal to $\pi/2-\theta_P$. The two other angles can be obtained by taking the first column of the Euler rotation matrix, which provides the components of the unit vector x' in the reference N,W,Z$^+$ basis (noted xyz hereafter) after the Euler rotation. This can be written as

$$\mathbf{e}_{x'} = (\cos\psi\cos\phi - \sin\psi sin\phi\cos\theta)\mathbf{e}_x + (\sin\psi\cos\phi + \cos\psi\sin\phi\cos\theta)\mathbf{e}_y + \sin\theta\sin\phi\mathbf{e}_z. \tag{5}$$

The scalar product of this vector with the vertical axis is by definition the cosine of the Incidence, so we have

$$\cos(I_P) = \sin(\theta)\sin(\phi). \tag{6}$$

We then get the azimuth by computing the scalar product of the horizontal projection of $\mathbf{e}_{x'}$ (with normalization to 1) on North, which gives

$$\cos(\psi_P) = \frac{\cos\psi\cos\phi - \sin\psi\cos\theta\sin\phi}{\sqrt{\cos^2\phi + \cos^2\theta\sin^2\phi}}, \tag{7}$$

We have also :

$$\cos(\psi_P) = \cos(\psi + \delta\psi) = \cos(\psi)\cos(\delta\psi) - \sin(\psi)\sin(\delta\psi) \tag{8}$$

By analogy between equation (6) and (7) we get:

$$\cos(\delta\psi) = \frac{\cos(\phi)}{\sqrt{\cos^2\phi + \cos^2\theta\sin^2\phi}} \tag{9}$$

and

$$\sin(\delta\psi) = \frac{\cos(\theta)\sin(\phi)}{\sqrt{\cos^2\phi + \cos^2\theta\sin^2\phi}} \tag{10}$$

and finally $\tan\delta\psi = cos\theta \tan\phi$ and we get the last and third Euler angle. Let us now assume that the particle motion is expressed as a vertical/horizontal elliptical motion and a linearly polarized one, the later having a phase delay ϕ_N with respect to the vertical amplitude of the elliptical motion. In the (xyz) frame, we can express the particle motion after Euler rotation on the three components as:

$$x = E_{xx}A\cos(\omega t) + E_{xy}A(1-L)\sin(\omega t) \ , \quad (11)$$
$$y = E_{yx}A\cos(\omega t) + E_{yy}A(1-L)\sin(\omega t) \ , \quad (12)$$
$$z = E_{zx}A\cos(\omega t) + E_{zy}A(1-L)\sin(\omega t) \ , \quad (13)$$

where E_{ij} are the elements of the Euler rotation matrix. Same particle motion can be written as the composition of the two (linear and elliptical) motions:

$$x = H_x\sin(\omega t) + N\cos\psi_N\cos(\omega t-\phi_N) \ , \quad (14)$$
$$y = H_y\sin(\omega t) + N\sin\psi_N\cos(\omega t-\phi_N) \ , \quad (15)$$
$$z = Z\cos(\omega t) + N_z\cos(\omega t-\phi_N) \ , \quad (16)$$

where H_x, H_y,Z, N, ψ_N, N_z are the x, y components of the elliptical motion, the z' component of the elliptical motion, the horizontal linear motion, the azimuth of the horizontal motion and the vertical linear motion respectively. After replacing , these six components can be determined by equating the 6 cosine and sin equations as functions of A, of the 4 parameters of the particle motion in the Oxyz (L,ψ_P,θ_P,I_P) and of the phase delay parameter ϕ_N between the elliptical and linear motions. We then get:

$$\begin{aligned}
tan(\psi_N) &= \frac{E_{yx}}{E_{xx}} \ , \\
\frac{N}{A} &= \frac{\sqrt{E_{xx}^2+E_{yx}^2}}{cos(\phi_N)} \ , \\
\frac{H_x}{A} &= E_{xy}(1-L) - \frac{N}{A}\cos(\psi_N)\sin(\phi_N) \ , \\
\frac{H_y}{A} &= E_{yy}(1-L) - \frac{N}{A}\sin(\psi_N)\sin(\phi_N) \ , \\
\frac{N_z}{A} &= \frac{E_{zy}(1-L)}{\sin(\phi_N)} \ , \\
\frac{Z}{A} &= E_{zx} - \frac{E_{zy}(1-L)}{\tan(\phi_N)} \ .
\end{aligned}$$

We note that smaller is the phase shift ϕ_N, larger will be the vertical components of the linear motion, as it is the only one matching the sin component on the vertical component. The azimuth with respect to North in the N,E of the horizontal components of the elliptical polarized motion is $tan(\psi_H) = -\frac{H_y}{H_x}$ while the one of the linear component will be $-\phi_N$. All components for Z downward are the opposite for N_z and Z.

References

Aki, K. (1992). Scattering conversions-p to conversion-s versus-s to versus-p. *Bulletin of the Seismological Society of America*, *82*(4), 1969-1972.

Aki, K., & Richards, P. G. (2002). *Quantitative Seismology* (J. Ellis, Ed.). University Science Books.

Anderson, D. L., Miller, W., Latham, G., Nakamura, Y., Toksöz, M., Dainty, A., ... Knight, T. (1977). Seismology on mars. *Journal of Geophysical Research*, *82*(28), 4524-4546.

Ardhuin, F., Gualtieri, L., & Stutzmann, E. (2015). How ocean waves rock the earth: Two mechanisms explain microseisms with periods 3 to 300 s. *Geophysical Research Letters*, *42*(3), 765–772. doi: 10.1002/2014gl062782

Banerdt, B., Smrekar, S., Banfield, D., & al. (2020). Initial results from the insight mission on mars. *Nature Geoscience*, *13*, 183-189. doi: 10.1038/s41561-020-0544-y

Banfield, D., Spiga, A., Newman, C., & al. (2020). The atmosphere of mars as observed by insight. *Nature Geoscience*, *13*, 190-. doi: 10.1038/s41561-020-0534-0

Charalambous, C., Stott, A., Pike, W., McClean, W., Warren, T., Spiga, A., ... Banerdt, W. (2020). A comodulation analysis of atmospheric energy injection into the ground motion at insight, mars. *Earth and Space Science Open Archive*, TBD. doi: 10.1002/essoar.10503206.1

Crawford, W. C., Webb, C., Spahr, & Hildebrand, J. A. (1991). Seafloor compliance observed by long-period pressure and displacement measurements. *Journal of Geophysical Research: Solid Earth*, *96*(B10), 16151–16160.

Cuxart, J., Tatrai, D., Weidinger, T., Kircsi, A., Jozsa, J., & Kiss, M. (2016). Infrasound as a Detector of Local and Remote Turbulence. *BOUNDARY-LAYER METEOROLOGY*, *159*(2), 185-192.

Farrell, W. (1972). Deformation of the earth by surface loads. *Reviews of Geophysics*, *10*(3), 761–797.

Garcia, R. P., Kenda, R., Kawamura, T., Spiga, A., N., M., Lognonné, P., ... Banerdt, B. (2020). Pressure effects on the seis-insight instrument, improvement of the seismic records and charcatrizaton of the long period atmospheric waves from ground displacement. *Journal of Geophysical Research: Planets*. doi: 10.1029/2019JE006278

Giardini, D., Lognonne, P., Banerdt, W., Pike, W., Christenseni, U., & al. (2020). The seismicity on mars. *Nature Geoscience*, *13*, 205-212. doi: 10.1038/s41561-020-0539-8

Goldreich, P., & Keeley, D. (1977). Solar seismology. ii-the stochastic excitation of the solar p-modes by turbulent convection. *The Astrophysical Journal*, *212*, 243–251.

Golombek, M., Warner, N., Grant, J., & al. (2020). Geology of the insight landing site, mars. *Nature Geoscience*, *11*, 1014. doi: 10.1038/s41467-020-14679-1

Gualtieri, L., Stutzmann, É., Farra, V., Capdeville, Y., Schimmel, M., Ardhuin, F., & Morelli, A. (2014). Modelling the ocean site effect on seismic noise body waves. *Geophysical Journal International*, *197*(2), 1096–1106. doi: 10.1093/gji/ggu042

Hasselmann, K. (1963). A statistical analysis of the generation of microseisms. *Rev. Geophys.*, *1*, 177-209.

Haubrich, R. A., & McCamy, K. (1969). Microseisms: Coastal and pelagic sources. *Reviews of Geophysics*, *7*(3), 539–571.

Kenda, B., Drilleau, M., Garcia, R., Kawamura, T., Murdoch, N., Compaire, N., ... Widmer-Schnidrig, R. (2020). Subsurface structure at the insight landing site from compliance measurements by seismic and meteorological experiments. *J. Geophys. Res.* doi: 10.1029/2020JE006387

Kenda, B., Lognonné, P., Spiga, A., Kawamura, T., Kedar, S., Banerdt, W. B., ... Golombek, M. (2017). Modeling of ground deformation and shallow surface waves generated by martian dust devils and perspectives for near-surface structure inversion. *Space Science Reviews*, *211*(1-4), 501-524. doi: 10.1007/s11214-017-0378-0

Lognonne, P., Banerdt, W., W.T.Pike, Giardini, D., Christensen, U., & al. (2020). Constraints on the shallow elastic and anelastic structure of mars from insight seismic data. *Nature Geoscience*, *13*, 213-220. doi: 10.1038/s41561-020-0536-y

Lognonne, P., Banerdt, W. B., Giardini, D., Pike, W. T., Christensen, U., Laudet, P., ... et al. (2019). Seis: Insight's seismic experiment for internal structure of mars. *Space Science Reviews*, *215*(1). doi: 10.1007/s11214-018-0574-6

Lognonné, P., & Mosser, B. (1993). Planetary seismology. *Surveys in Geophysics*, *14*(3), 239-302. doi: 10.1007/BF00690946
Lorenz, R., Kedar, S., Murdoch, N., Lognonné, P., Kawamura, T., Mimoun, D., & Banerdt, B. (2015). Seismometer signature of dust devils: implication for insight. In *European planetary science congress* (Vol. 10).
Martire, L., Garcia, R. F., Rolland, L., Spiga, A., Lognonné, P., Banfield, D., ... Martin, R. (2020). Martian infrasound: Numerical modeling and analysis of insight's data. *Journal of Geophysical Research: Planets*, *n/a*(n/a), e2020JE006376. Retrieved from `https://agupubs.onlinelibrary.wiley.com/doi/abs/10.1029/2020JE006376` (e2020JE006376 2020JE006376) doi: 10.1029/2020JE006376
Mimoun, N., D.and Murdoch, Lognonné, P., Hurst, K., Pike, T., Hurley, J., Nébut, T., ... Team, S. (2017). The noise model of the seis seismometer of the insight mission to mars. *Space Science Reviews*, *211*(1-4), 383-428. doi: 10.1007/s11214-017-0409-x
Murdoch, N., D., A., B., K.-E., Teanby, N. A., & Myhill, R. (2018). Flexible mode modelling of the insight lander and consequences for the seis instrument. *Space Science Reviews*, *214*(117), 1–24. doi: 10.1007/s11214-018-0553-y
Murdoch, N., Kenda, B., Kawamura, T., Spiga, A., Lognonné, P., Mimoun, D., & Banerdt, B. (2017). Estimations of the seismic pressure noise on mars determined from large eddy simulations and demonstration of pressure decorrelation techniques for the insight mission. *Space Science Reviews*, *211*(1-4), 457-483.
Nishikawa, Y., Lognonné, P., Kawamura, T., Spiga, A., Stutzmann, E., Schimmel, M., ... Kurita, K. (2019). Mars' background free oscillations. *Space Science Reviews*, *215*(1). doi: 10.1007/s11214-019-0579-9
Panning, M. P., Pike, W. T., Lognonné, P., Banerdt, W. B., Murdoch, N., Banfield, D., ... others (2020). On-deck seismology: Lessons from insight for future planetary seismology. *Journal of Geophysical Research: Planets*, e2019JE006353.
Papanicolaou, G., Ryzhik, L., & Keller, J. (1996). Stability of the P-to-S energy ratio in the diffusive regime (vol 86, pg 1107, 1996). *BULLETIN OF THE SEISMOLOGICAL SOCIETY OF AMERICA*, *86*(6).
Peterson, J. (1993). Observations and modeling of seismic background noise. *U.S. Geol. Surv. Tech. Rept.*, *93*(322).
Posmentier, E. (1974). 1-HZ to 16-HZ infrasound associated with clear air turbulence predictor . *Journal of Geophysical research*, *79*(12), 1755-1760. doi: 10.1029/JC079i012p01755
Romero, P., & Schimmel, M. (2018, Jun). Mapping the basement of the ebro basin in spain with seismic ambient noise autocorrelations. *Journal of Geophysical Research: Solid Earth*, *123*(6), 5052–5067. doi: 10.1029/2018jb015498
Roult, G., & Crawford, W. (2000). Analysis of 'background'free oscillations and how to improve resolution by subtracting the atmospheric pressure signal. *Physics of the Earth and Planetary Interiors*, *121*(3-4), 325–338.
Samson, J., & Olson, J. (1980). Some comments on the descriptions of the polarization states of waves. *Geophys. J. R. astr. Soc.*, *61*.
Schimmel, M., & Gallart, J. (2003). The use of instantaneous polarization attributes for seismic signal detection and image enhancement. *Geophysical Journal International*, *155*(2), 653–668.
Schimmel, M., & Gallart, J. (2004). Degree of polarization filter for frequency-dependent signal enhancement through noise suppression. *Bulletin of the Seismological Society of America*, *94*(3), 1016–1035.
Schimmel, M., Stutzmann, E., Ardhuin, F., & Gallart, J. (2011b). Polarized earth's ambient microseismic noise. *Geochem. Geophys. Geosyst.*(12), Q07014. doi: 10.1029/2011GC003661
Schimmel, M., Stutzmann, E., & Gallart, J. (2011a). Using instantaneous

phase coherence for signal extraction from ambient noise data at a local to a global scale. *Geophysical Journal International*, *184*(1), 494–506. doi: 10.1111/j.1365-246x.2010.04861.x

Scholtz, J.-R., Widmer-Schnidrig, R., Davis, P., Lognonné, P., Pinot, B., Garcia, R., ... Banerdt, W. B. (2020). Detection, analysis and removal of glitches from insight's seismic data from mars. *J. Geophys. Res*, *2020JE006507*(-), -.

Shields, F. (2005, JUN). Low-frequency wind noise correlation in microphone arrays. *JOURNAL OF THE ACOUSTICAL SOCIETY OF AMERICA*, *117*(6), 3489-3496. (145th Annual Conference of the Acoustical-Society-of-America, Nashville, TN, APR 28-MAY 02, 2003)

Sorrells, G. G. (1971). A preliminary investigation into the relationship between long-period seismic noise and local fluctuations in the atmospheric pressure field. *Geophysical Journal International*, *26*(1-4), 71–82.

Spiga, A., Banfield, D., Teanby, N. A., Forget, F., Lucas, A., Kenda, B., ... et al. (2018). Atmospheric science with insight. *Space Science Reviews*, *214*(7). doi: 10.1007/s11214-018-0543-0

Stockwell, R. G., Mansinha, L., & Lowe, R. P. (1996). Localization of the complex spectrum: the S transform. *IEEE Trans. Signal Process.*, *44*(4), 998–1001.

Stutzmann, E., Ardhuin, F., Schimmel, M., Mangeney, A., & Patau, G. (2012, Sep). Modelling long-term seismic noise in various environments. *Geophysical Journal International*, *191*(2), 707–722. doi: 10.1111/j.1365-246x.2012.05638.x

Stutzmann, E., Schimmel, M., Patau, G., & Maggi, A. (2009, Nov). Global climate imprint on seismic noise. *Geochemistry, Geophysics, Geosystems*, *10*(11), n/a–n/a. doi: 10.1029/2009gc002619

Tanimoto, T., Ishimaru, S., & Alvizuri, C. (2006). Seasonality in particle motion of microseisms. *Geophysical Journal International*, *166*(1), 253–266. doi: 10.1111/j.1365-246x.2006.02931.x

Tanimoto, T., & Rivera, L. (2005). Prograde rayleigh wave particle motion. *Geophysical Journal International*, *162*(2), 399-405.

Van Hoolst, T., Dehant, V., Roosbeek, F., & Lognonné, P. (2003). Tidally induced surface displacements, external potential variations, and gravity variations on mars. *Icarus*, *161*(2), 281–296. doi: 10.1016/S0019-1035(02)00045-3

Zhang, G., Hao, C., & Yao, C. (2018). Analytical study of the reflection and transmission coefficient of the submarine interface. *Acta Geophys.*, *66*(), 449-460. doi: {10.1007/s11600-018-0153-y}

Zürn, W., & Wielandt, E. (2007, Feb). On the minimum of vertical seismic noise near 3 mhz. *Geophysical Journal International*, *168*(2), 647–658. doi: 10.1111/j.1365-246x.2006.03189.x

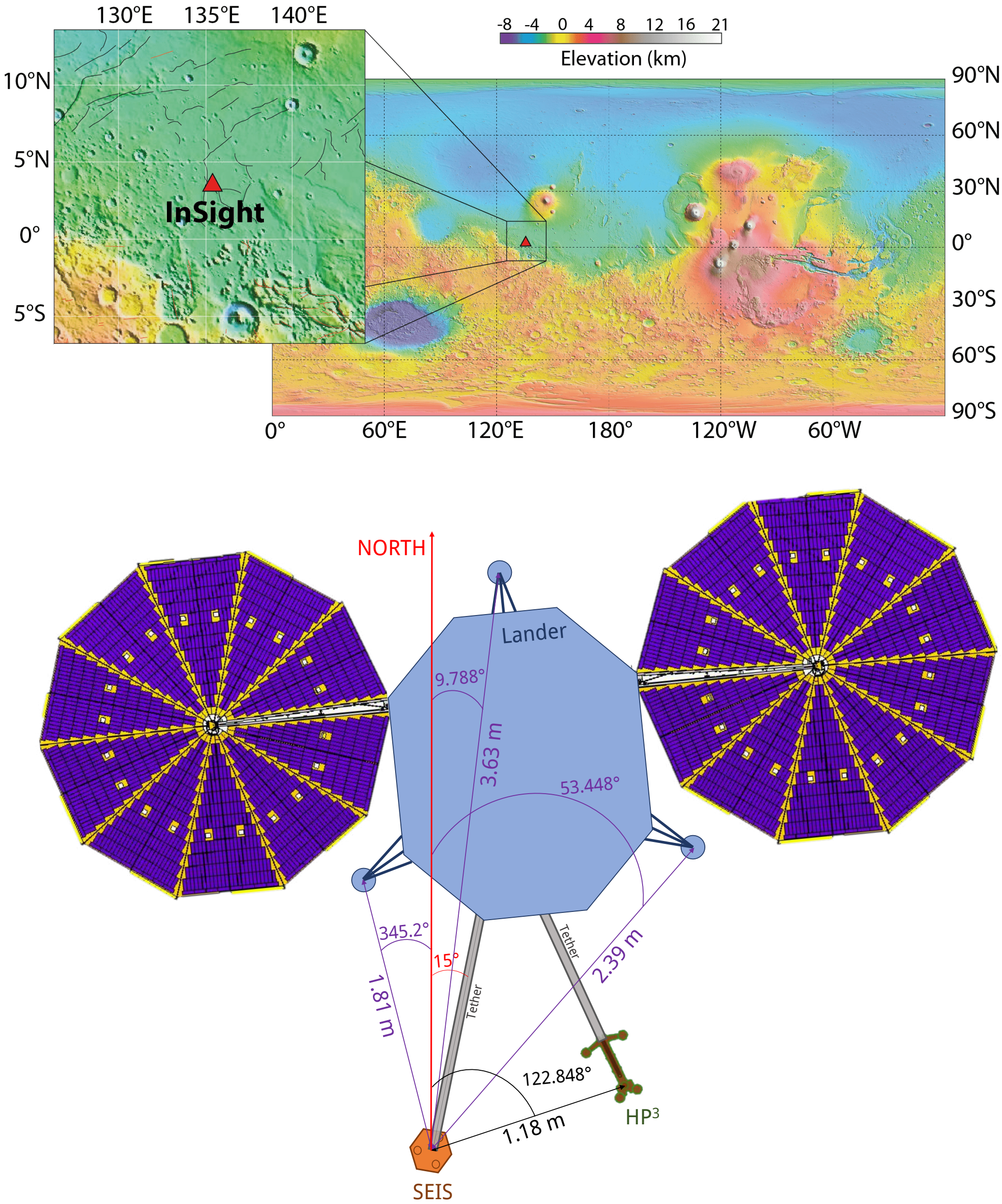

Figure 1. Insight lander and seismic station on Mars. The top plot shows Insight location (red triangle) on Mars topography map. The bottom plot is a sketch of the station and gives the position of the seismometer SEIS (orange) with respect to the lander (light blue) and its 3 feet (small circles) and with respect to HP3 instrument (brown). The 2 solar panels attached to the lander are in dark blue and yellow.

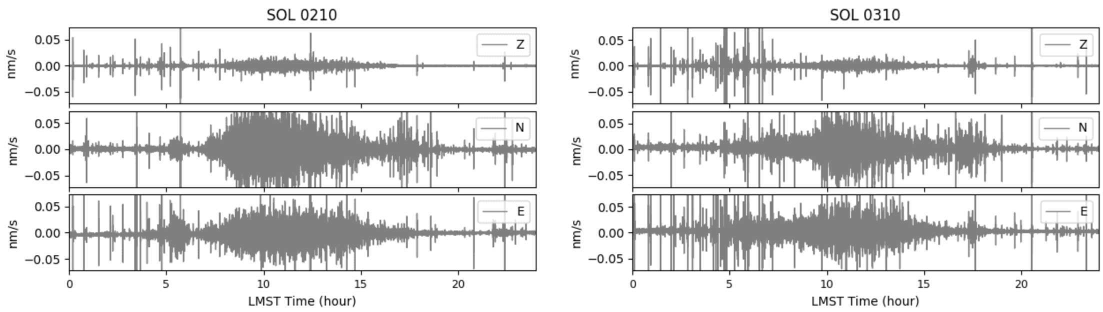

Figure 2. Continuous signals recorded by the 3 components of Insight broadband seismometer on Mars (top: Z, middle: N , bottom: E). on sol 210 (left) and 310 (right) filtered between 0.03 and 1 Hz.

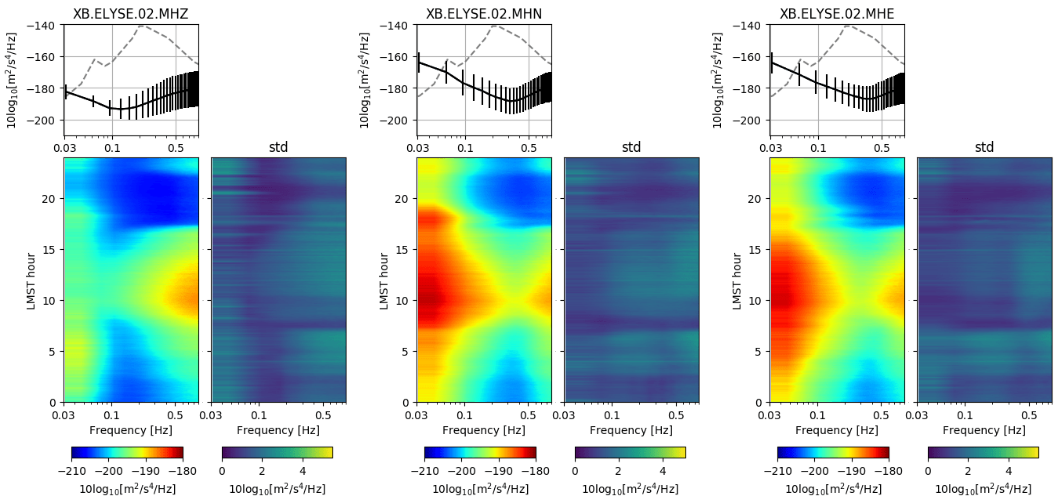

Figure 3. Average noise level recorded on Mars by the 3 components of Insight broadband seismometer (left: Z, middle: N , right: E) computed over sol 82 to 491. Top: average power spectrum density in dB with respect to acceleration as a function of frequency. Earth low noise model from (Peterson, 1993) is shown in dashed lines. Bottom: average spectrogram as a function of Mars local hour and corresponding standard deviation.

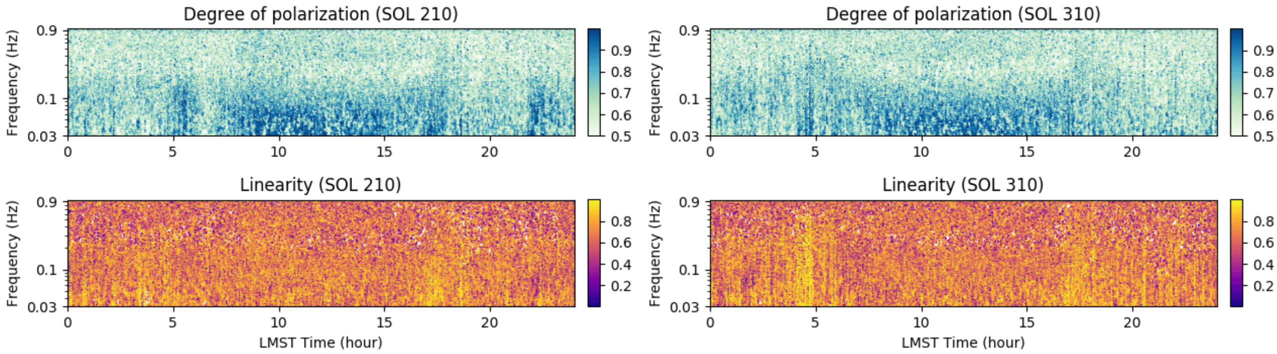

Figure 4. Degree of polarization, DOP, (top) and linearity (bottom) as a function of LMST time and frequency for sol 210 (left) and 310 (right). A higher DOP means that the signal polarization is more stable within the considered time-frequency window.

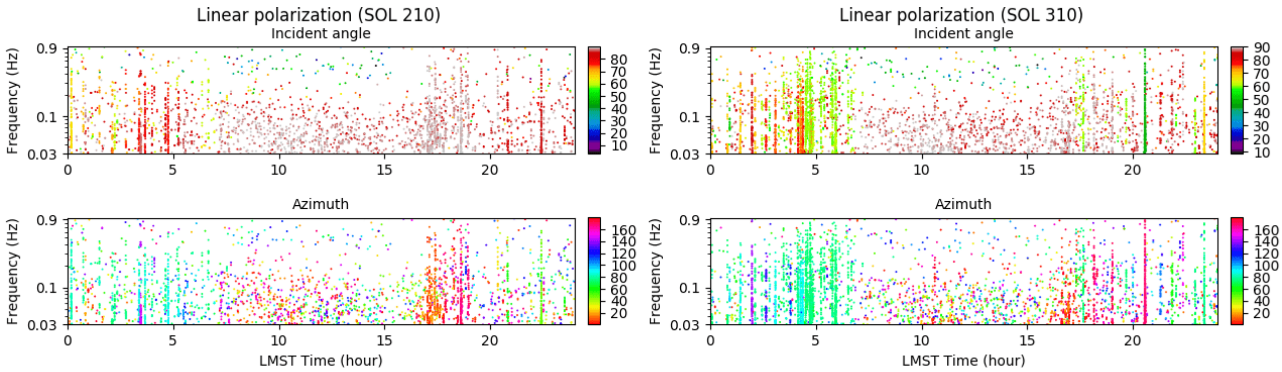

Figure 5. Incident angle and azimuth of signals with linear polarization as a function of LMST time and frequency for sol 210 (left) and 310 (right). The colours mark the incident and azimuth angles in degree and are measured from the vertical and the North over East, respectively.

a.

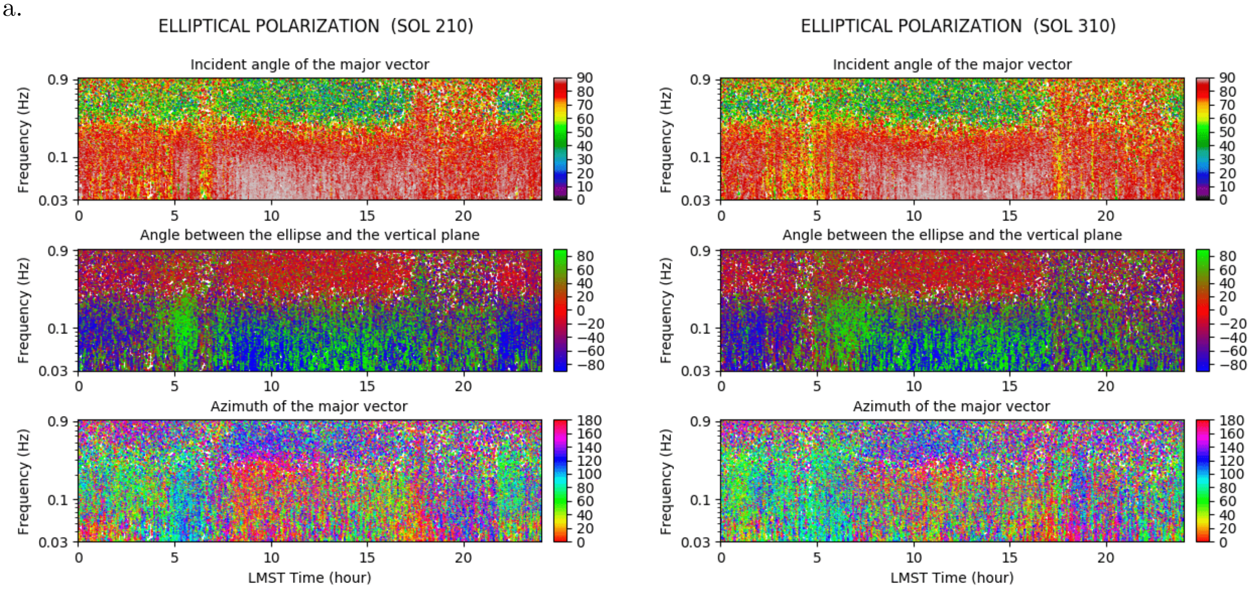

b.

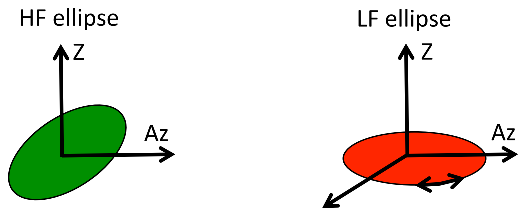

Figure 6. For signals with elliptical polarization, incident angle of the major axis (a. top), angle between the ellipse and the vertical plane (a. middle) and azimuth of the major vector (a. bottom) as a function of LMST time and frequency for sol 210 (a. left) and 310 (a. right). Angles are all in degrees. Azimuth are between 0 and 180° with an undetermination of 180°. A sketch of the high frequency and low frequency ellipse of polarization is shown in b.

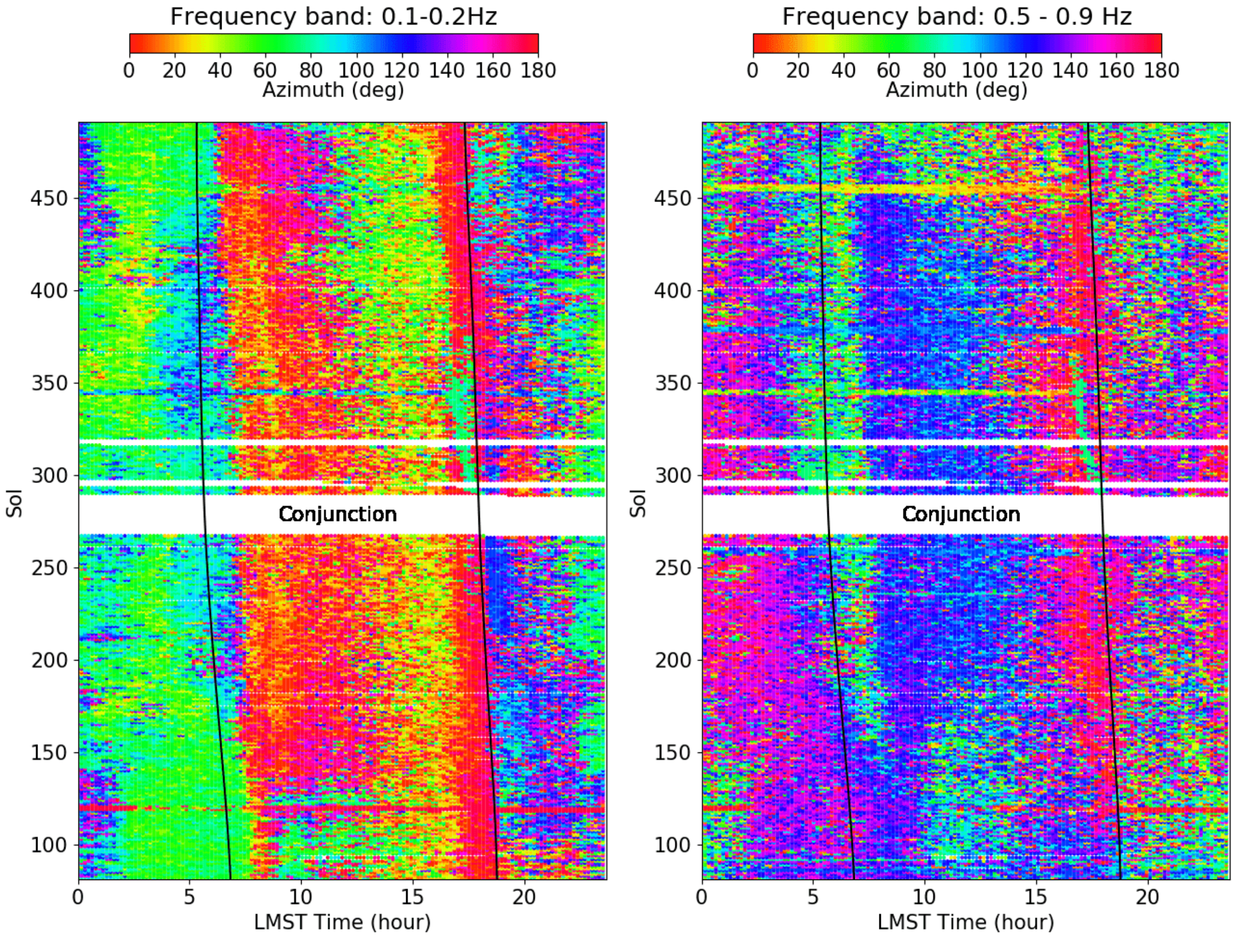

Figure 7. For signals with elliptical polarization, azimuth of the particle motion as a function of LMST time for sols 85 to 365, every 5 sols. Frequency bands are 0.1-0.2 Hz (left) and (0.5-0.9 Hz (right). Summer solstice is on sol 308. Data were not available during the conjunction. Black lines indicate sunrise and sunset times each sol.

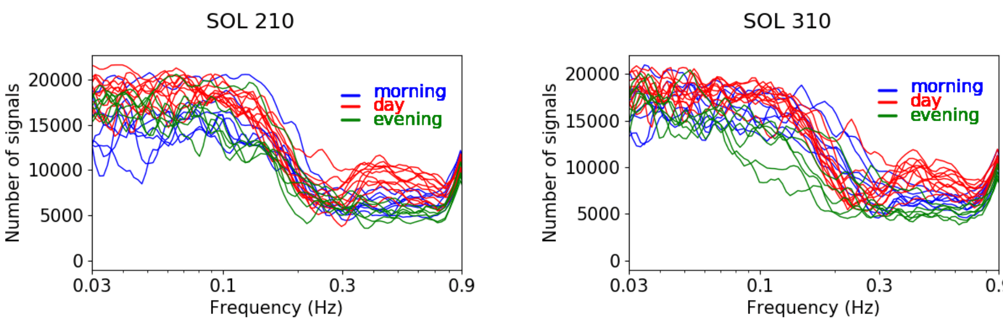

Figure 8. Number of polarized signals detected per hour as a function of frequency in the morning (0:00-7:00, blue curves), during the day (7:00-18:00,red curves) and the evening (18:00-24:00, green curves) on sol 210 (left) and 310 (right).

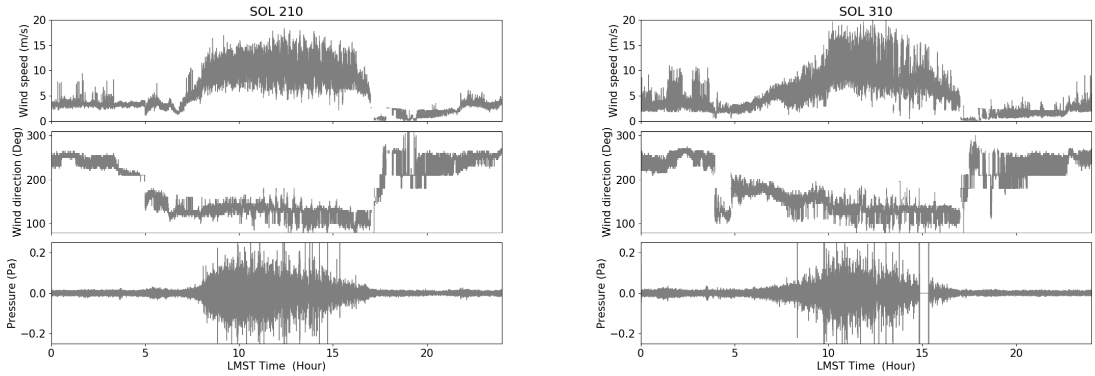

Figure 9. For sol 210 (left) and 310 (right), wind speed, wind direction and pressure. Pressure is band-pass filtered between 0.03 and 0.99 Hz to be compared with seismic data. Sunrise is at 6:01 and 5:35 and sunset at 18:14 and 17:53, for sol 210 and 310 respectively.

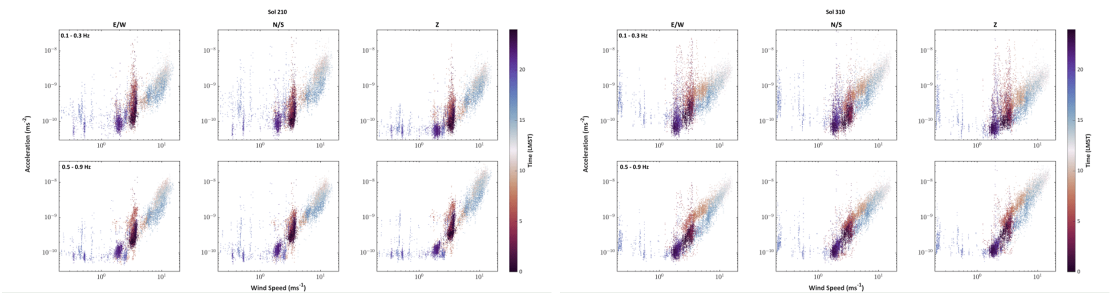

Figure 10. Seismic amplitude rms in acceleration as a function of local wind speed and LMST for each component E/W, N/S and vertical in the frequency band 0.1-0.3 Hz (top row) and 0.5-0.9 Hz (bottom row). Sol 210 is shown on the left and sol 310 on the right. Colors corresponds to the LMST hours.

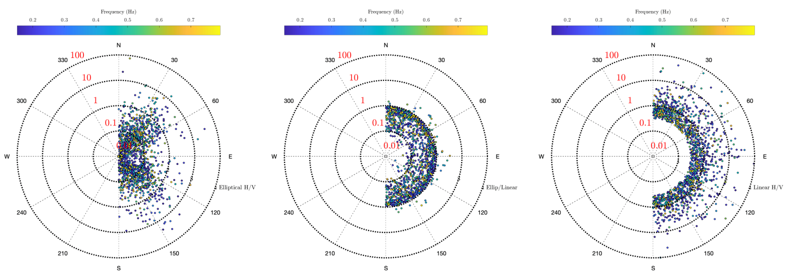

Figure 11. Decomposition of the elliptically polarized signals from sol 210 into elliptical and linear components assuming a phase delay of 0.15 radians between both components. From left to right are shown the H/V ratio of the elliptical components, the ratio between elliptical and linear component and the H/V ratio of the linear component. Only polarized signals for degree of polarization larger than 0.75, frequencies between 0.15 Hz and 0.8 Hz and linearity between 0.85 and 0.95 (B/A ratio between 0.05 and 0.15). This corresponds to signals with small but stable ellipticity. For this selected phase shift, a significant amount of the elliptical component is found along the 30-40 degree North azimuth and its perpendicular direction. Both the elliptical and linear component have signals with H/V ratio below one than above. Most of the signals have more energy on the linear component than on the elliptical component, tending toward equivalent energy at 0.8 Hz.

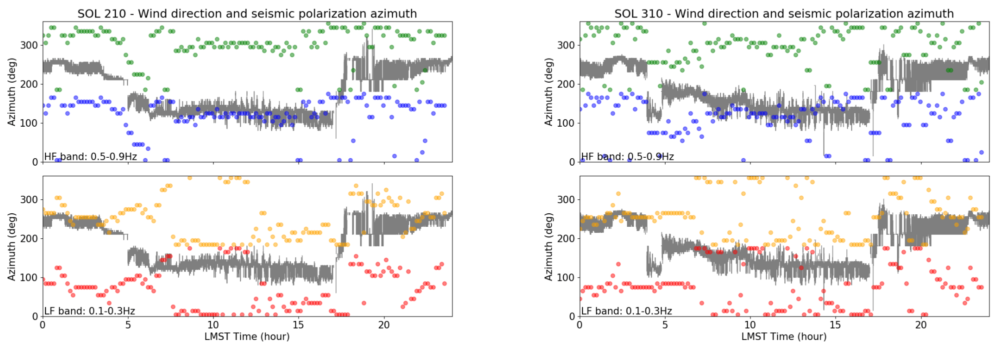

Figure 12. Polarization azimuths (color) in the frequency band 0.5-0.9 Hz (top) and 0.1-0.3 Hz (bottom) and wind azimuth (grey) for sol 210 (left) and 310 (right). Measured azimuths are plotted in blue and red and these angles + 180° are in orange and green, respectively.

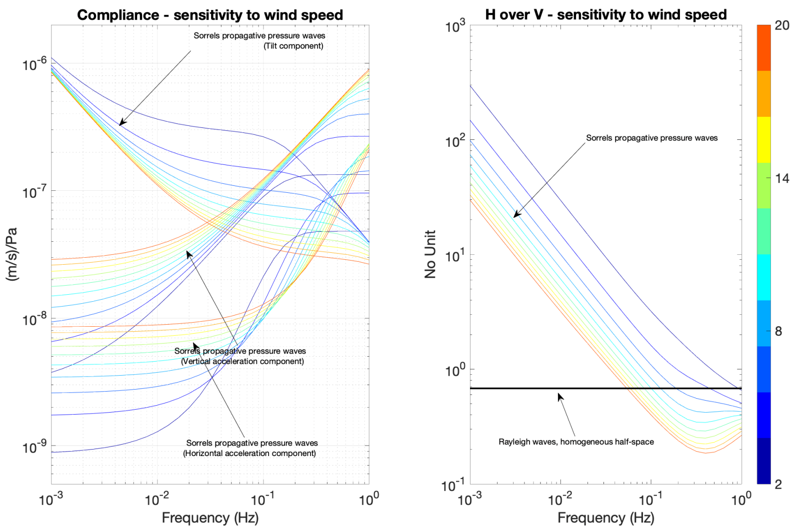

Figure 13. Vertical and horizontal compliances for the two layer model of Kenda et al. (2020). The first layer is 5 meters thick with Vp and Vs of 198 m/s and 118 m/s, while the second layer is a semi-infinite layer with Vp and Vs of 926 m/s and 512 m/s respectively. This model average the more complex model proposed by Lognonne et al. (2020). The horizontal acceleration is the sum of both the horizontal tilt and of the horizontal ground acceleration and converted in ground velocity. Together with the vertical ground velocity, they are shown for different wind velocities as a function of frequency on the left figure. The color bar represent the range of wind values, from 2 m/s to 20 m/s. The right figure shows the amplitude of the H/V ratio. The phase of the H/V for a layered model is the same as for an homogeneous model and equal to $-i$.
.

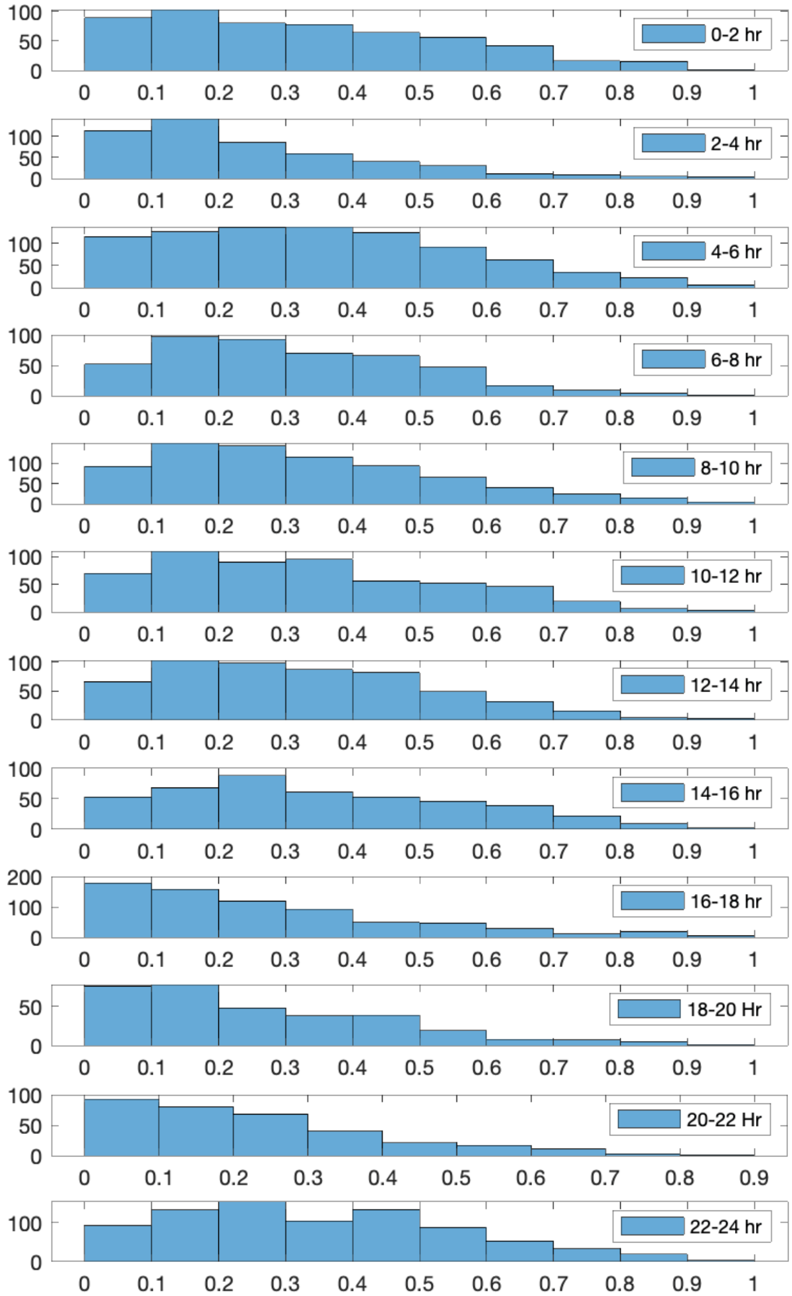

Figure 14. Histograms of the B/A ratio of the detected signals for sol 210 in the 0.1-0.2 Hz bandwidth. Only signals with degree of polarisation larger than 0.8 are shown. The smallest B/A signals are found during the very low wind regime, between 16:00 and 22:00 LMST. During the second part of the night, B/A values comparable to those during the day are found, despite lower wind. This might be related to more stable and steady flow regimes. Note that the wind parameter in Sorrells' theory is the environmental wind and not the instantaneous wind. This might reduce the differences between wind regime in the second part of the night and the day's one.

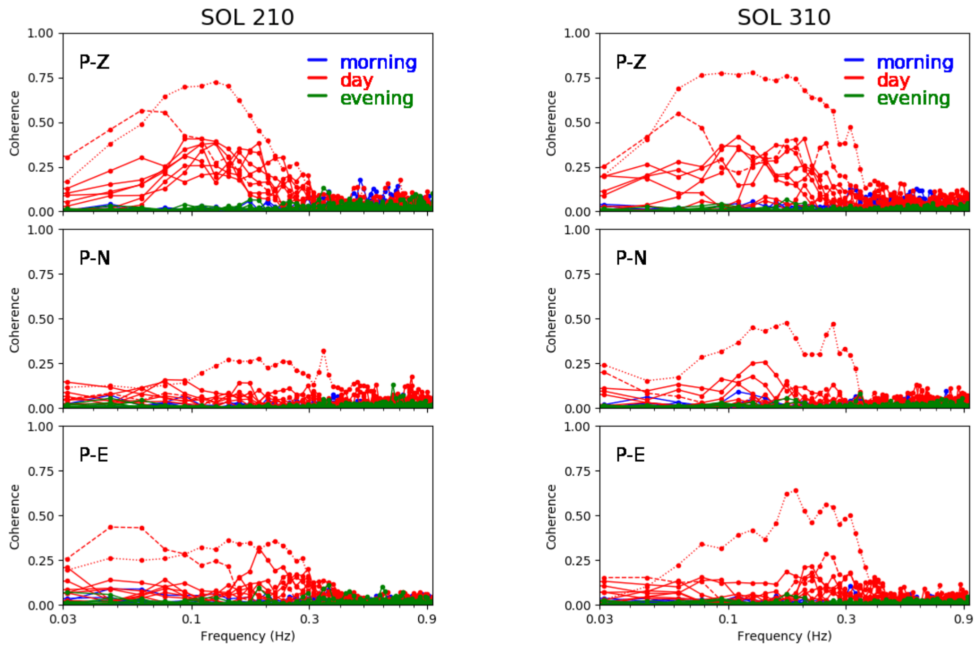

Figure 15. Coherence between pressure and seismic velocity as a function of frequency for each component: vertical (top) , N-S (middle), E-W (bottom) for sol 201 (left) and sol 310 (right), considering windows of one hour each. Dashed and dotted lines correspond to LMST hours 12 and 14 for sol 210, 13 and 9 for sol 310 for which coherence is the highest.

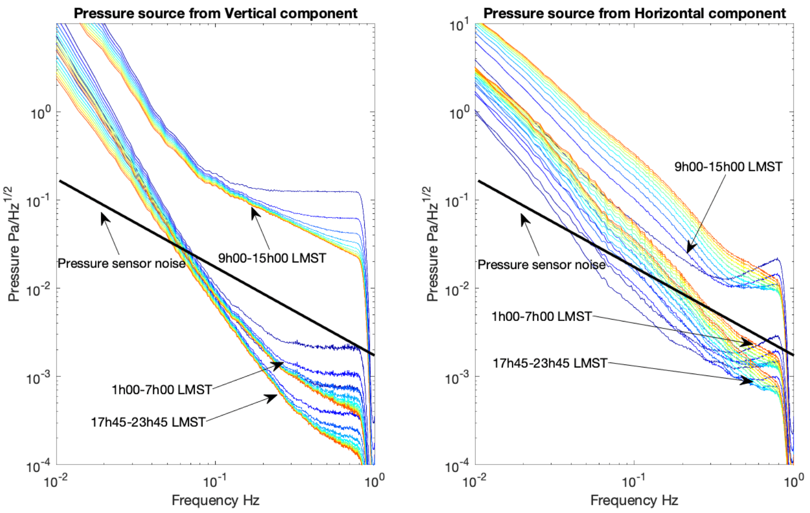

Figure 16. This figure provides the estimation of the pressure noise able to generate typical SEIS noise levels for different wind conditions. The three typical SEIS noise levels, from lowest to highest in acceleration spectral amplitude, are those of the late evening (17:45-23:45 LMST), night (1:00-7:00 LMST) and day (9:00-15:00), as provided by the supplement 1 of Lognonne et al. (2020). This is shown on the left for the vertical VBB component and on the right for the VBB horizontal component. The black line shows the lowest pressure noise spectra recorded by the InSight pressure sensor (Banfield et al., 2020). This shows that the SEIS noise, if due to pressure wave and above 0.1 Hz, needs for the vertical axis pressure much less than the resolution of the pressure sensor in the evening and night conditions. The necessary pressure on the horizontal components are however detectable for frequencies smaller than 0.2 Hz in the night. They are also always above the pressure sensor noise level during day conditions, which allows some pressure decorrelation during this period (Garcia et al., 2020)
.

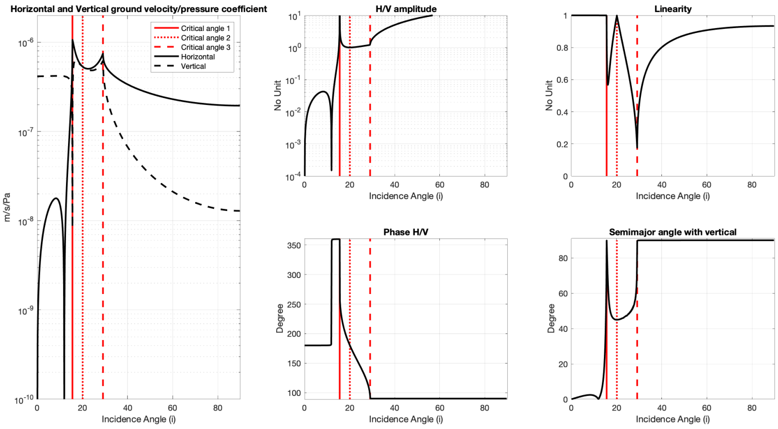

Figure 17. Transfer coefficient between the pressure amplitude of an acoustic wave and the horizontal and vertical ground velocity and impacts in terms of ground ellipticity. The left figure provides the transfer coefficient, as a function of incidence of the pressure wave with respect to vertical, between the amplitude of the pressure wave and the vertical and horizontal ground velocities for an simple interface between Mars atmosphere (with sound speed of 250 m/s and atmospheric density of 0.017 kg/m^3) and a breciated bedrock (Vp and Vs of 926 m/s and 512 m/s respectively and density of 2600 kg/m^3). The two critical angles and the one canceling the P transmited wave are detailed in the text are shown by the three red lines(first critical angle related to P, angle for no P transmission and second critical angle related to S). The two middle figures show the amplitude and phase of the H/V ratio, as a function of incidence angle. Below the first critical angle of 15.6 degree, the transfer coefficients are all real. They start to be complex after the first critical angle, with a variation from 360° to 90° of the H/V phase, until the second critical angle is reached, for an inclination of 29.1°. The phase remains after to 90°. The last panel shows the linearity and the inclination of the semi-major axis of the elliptical signal. For linearity of 1, the semi-major axis is the axis of linear polarization. When the incidence angle increase from the first critical angle to the incidence cancelling transmitted P, the linearity decreases down to about 0.6 before to reach again 1 for an incidence angle of 20.1°. The angle of the semi-major axis varies from 90° to 45° with respect to vertical. The same type of variation occurs between the 20.1° incidence and the second critical angle, with the linearity decreasing down to about 0.2 for the third critical angle and again a rotation of the semi-major axis. The semi-major axis remains vertically oriented after the second critical angle, while the linearity is growing toward 1 for large incidences.

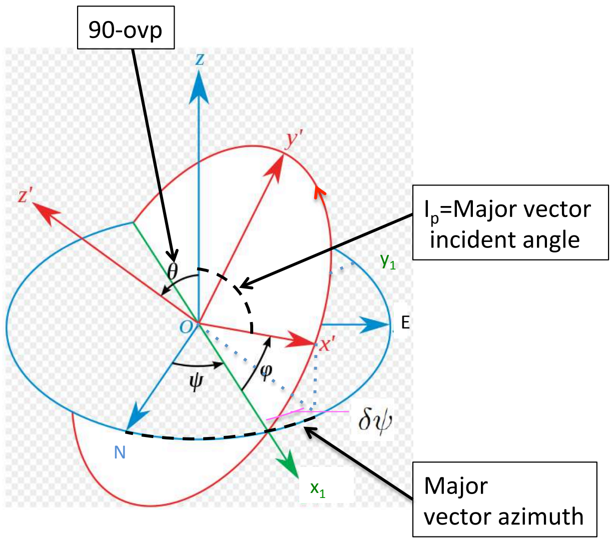

Figure 18. Sketch of the ellipse of polarization.The ellipse is defined by 3 angles: (1) the semi major vector azimuth with respect to North, (2) its incident angle with respect to the vertical and (3) the out of vertical plane angle, ovp. The motion in the ellipse plane is from x' toward y' as indicated by the red arrow. The Euler angles are Ψ, Φ and θ. Modified from wikipedia.

A Supplementary Material

Figure A1 to A4 show the azimuth of the measured signals with elliptical polarization as a function of LMST and frequency for 82 to 481. We see the discrepancy between high and low frequency and the progressive changes from one sol to another following seasonal changes. Some features such as the horizontal red lines on sol 118 to 121 are due to hammering next to the sensor for HP3 experiment.

Figure A5 and A6 display the spectrograms of the three seismic components for sol 210 and 310. We observe higher noise amplitude during the day and the lowermost amplitude in the evening between 1 and 3 sec of period. In this study we only investigated polarization in the frequency band 0.03-1 Hz and therefore the results are not affected by the resonance modes visible as yellow horizontal lines at higher frequency.

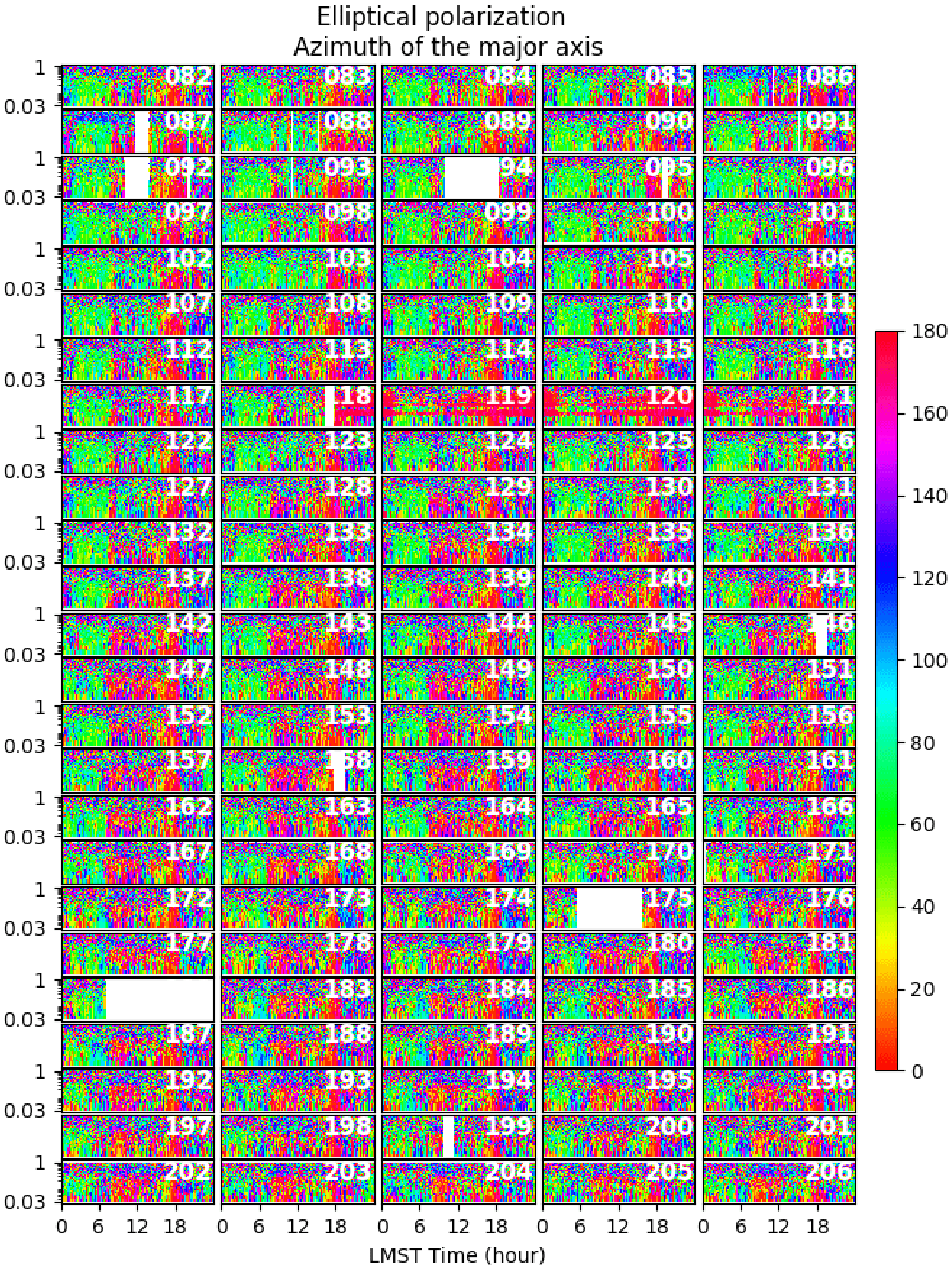

Figure A.1. For signals with elliptical polarization, azimuth of the particle motion as a function of LMST time and frequency for sols 82 to 206. Azimuth is measured in degree, clockwise from North.

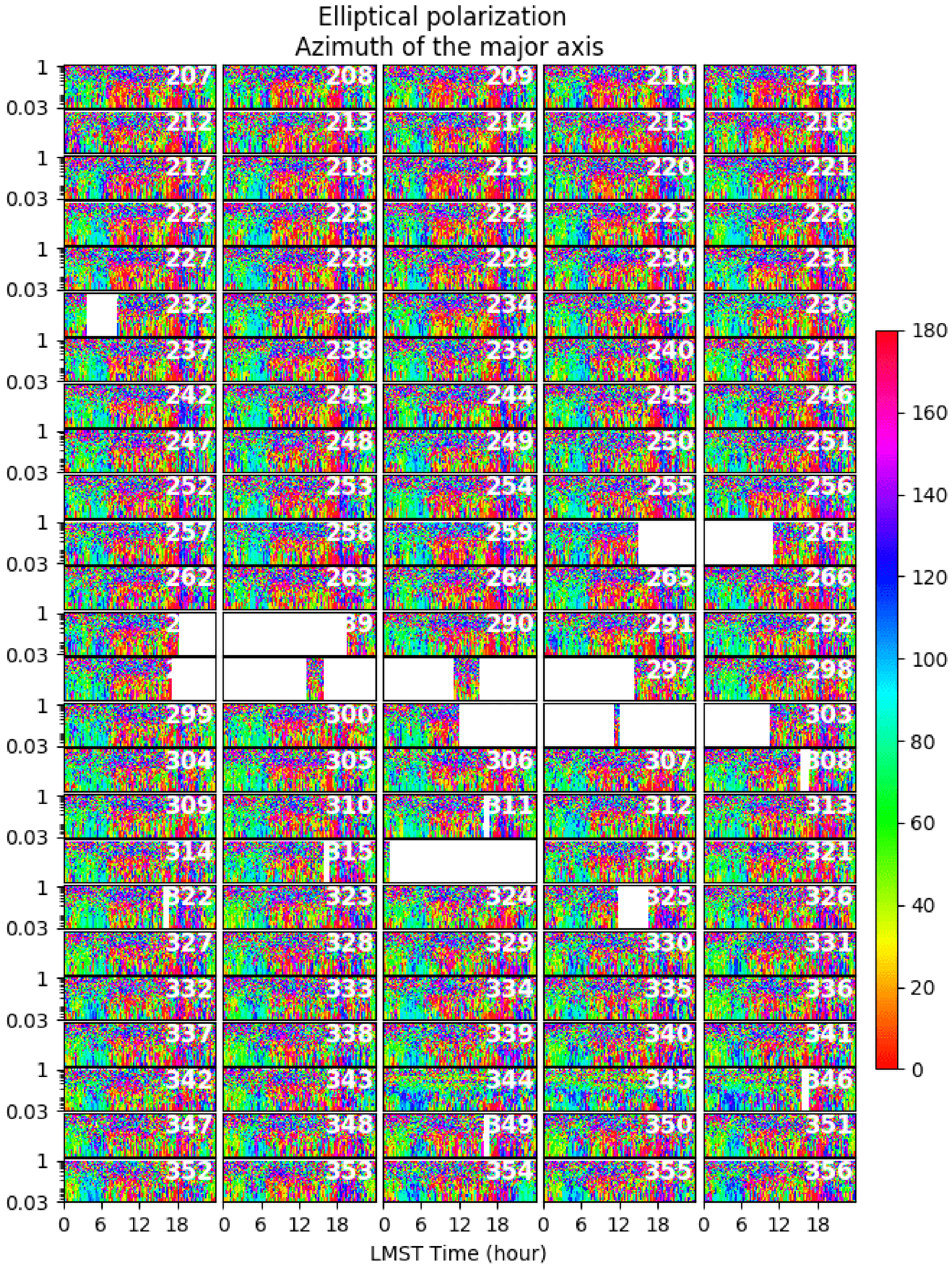

Figure A.2. For signals with elliptical polarization, azimuth of the particle motion as a function of LMST time and frequency for sols 207 to 356. Azimuth is measured in degree, clockwise from North.

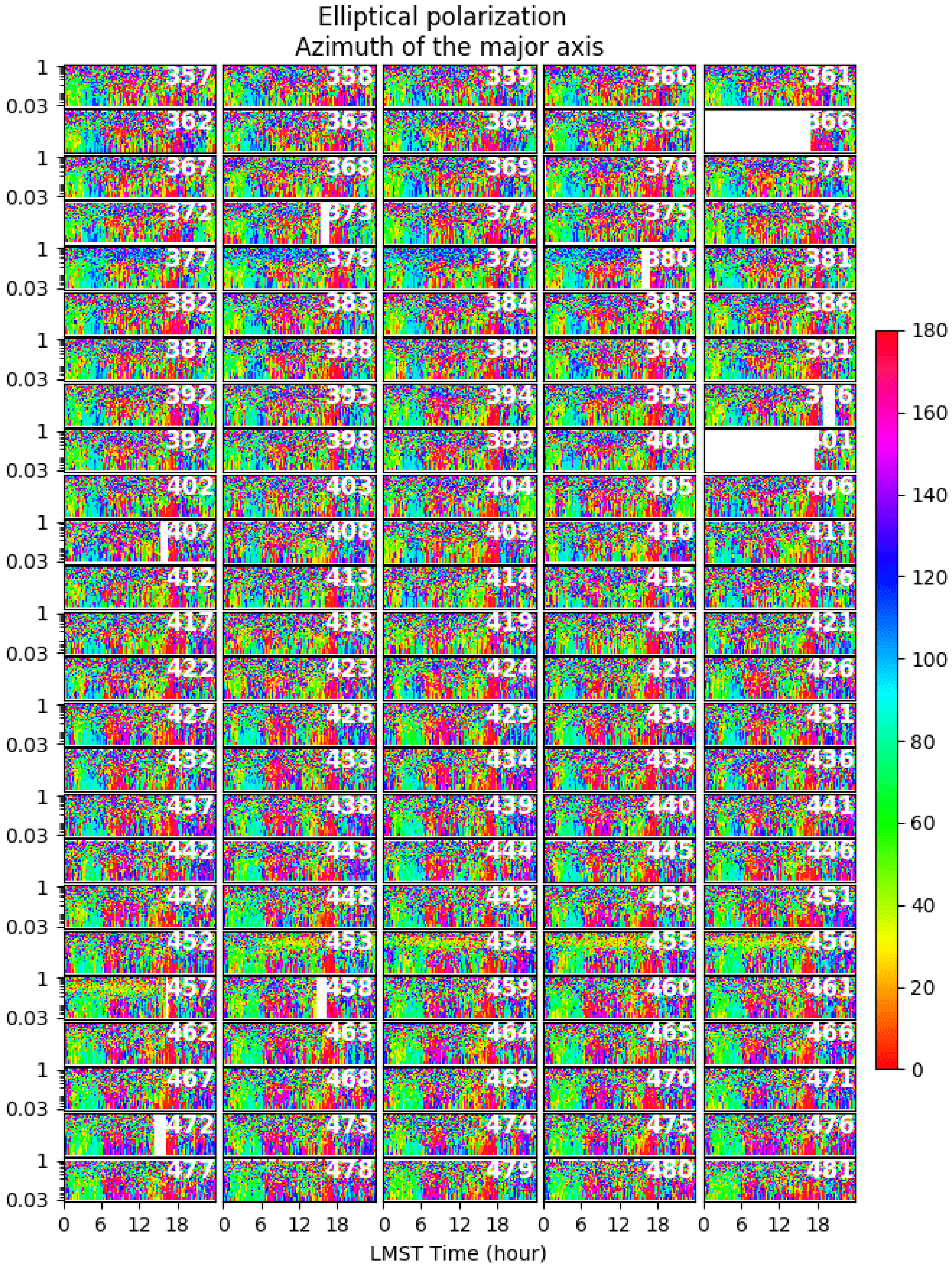

Figure A.3. For signals with elliptical polarization, azimuth of the particle motion as a function of LMST time and frequency for sols 357 to 481. Azimuth is measured in degree, clockwise from North.

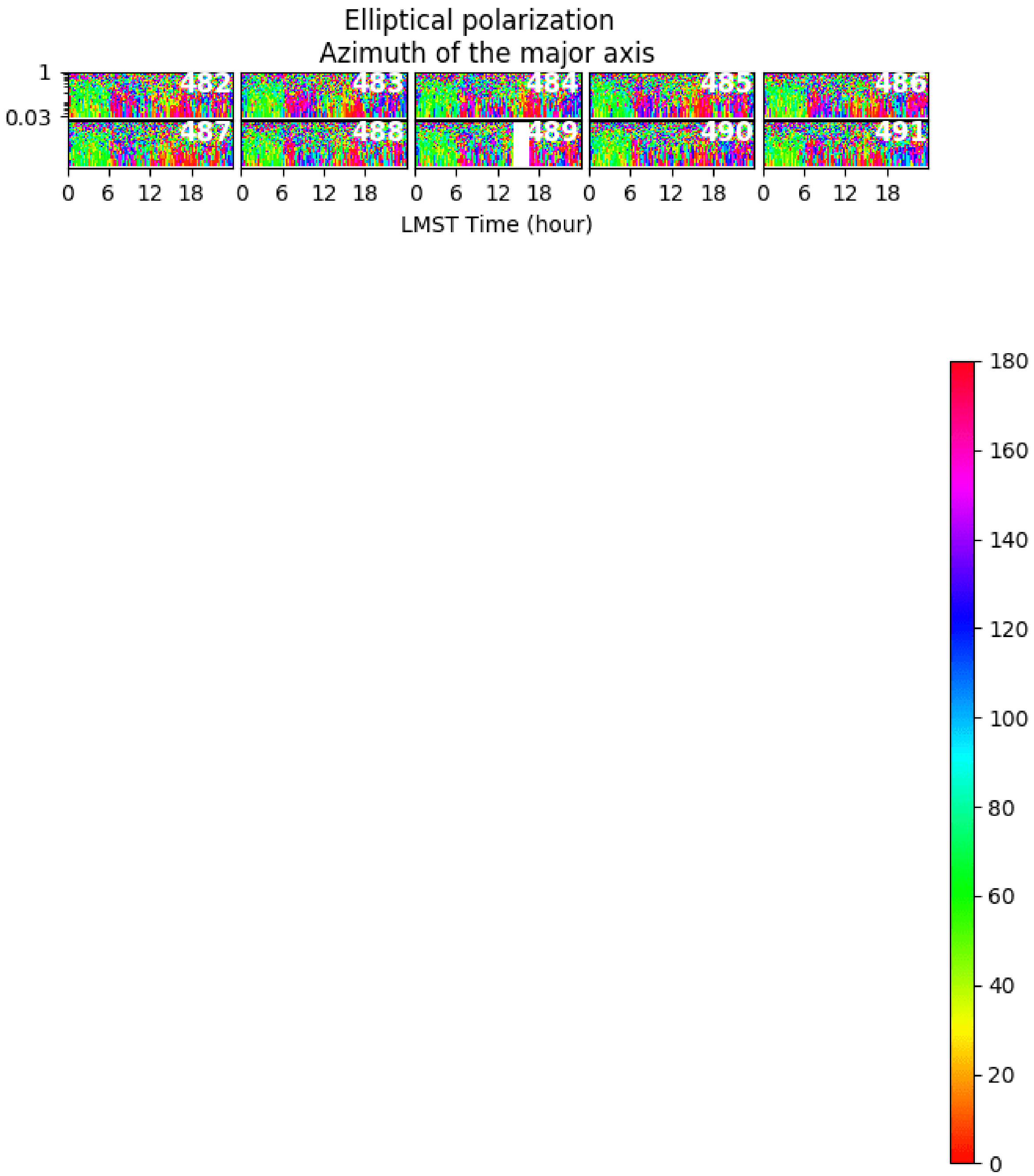

Figure A.4. For signals with elliptical polarization, azimuth of the particle motion as a function of LMST time and frequency for sols 482 to 491. Azimuth is measured in degree, clockwise from North.

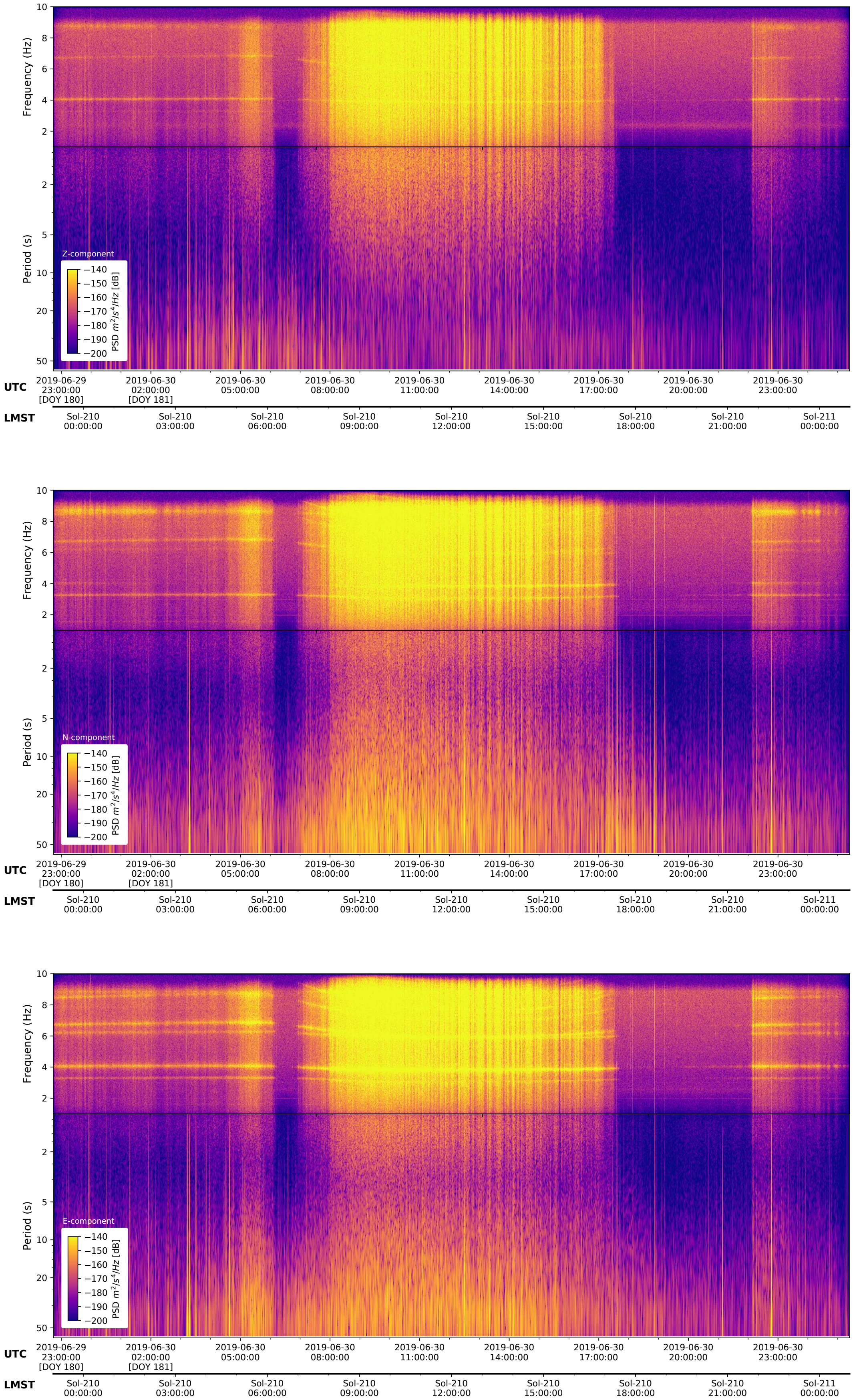

Figure A.5. Spectrogram of the ELYSE station seismic acceleration for the 3 components on sol 210.

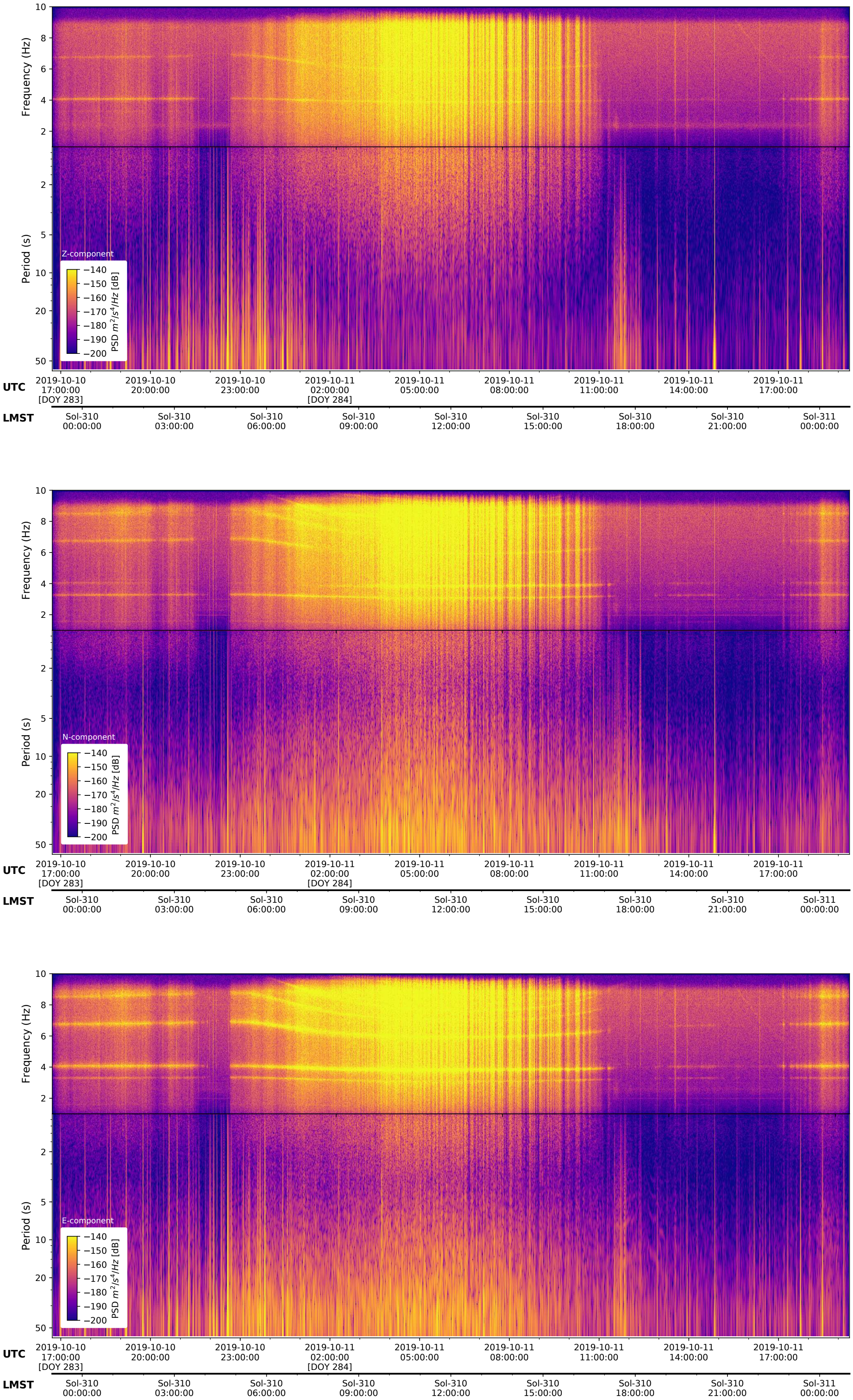

Figure A.6. Spectrogram of the ELYSE station seismic acceleration for the 3 components Z, N and E on sol 310.